Developing calibrated ultrasound equipment for sonoporation research

Torstein Yddal

Department of Physics and Technology

University of Bergen

A thesis submitted for the degree of

Master of Science

29 March 2014

Acknowledgements

I would like to start off by thanking my family, for their great support during my entire life. Without (some of) my fathers technical insight and my mothers impeccable tidiness, laboratory work would be a lot more challenging.

It is hard to express my gratitude to my great second supervisor and dear friend Dr. Spiros Kotopoulis. Without his endless support and patience, this thesis would never have been possible. His bottomless well of knowledge, never ceases to impress me, and it has certainly been a great honor to be working with and learning from him.

I would also like to thank my great supervisor Prof. Dr. Michiel Postema. For teaching me all about the fantastic world of non-linear acoustics and bubble dynamics, and supporting me throughout the thesis.

Furthermore, I would like to thank Prof. Dr. Per Lunde, for teaching me all the fundamentals of acoustics and ultrasonics.

I would also like to thank Ms. Laura Trachsel Moncho, for helping me understand the mechanisms of chemotherapy and cell biology. Her explanations and support has helped me a lot during the entire thesis.

I would like to thank The Michelsen Centre for Industrial Measurement Science and Technology. The study was supported by MedViz, a research cluster with groups from Haukeland University Hospital, University of Bergen and Christian Michelsen Research AS.

Abstract

Sonoporation is the transient formation of pores in cells, due to the application of ultrasound or ultrasound in combination with microbubbles. This increases drug uptake. Nevertheless, the ideal parameters for sonoporation have yet to be found. A major problem consists in the fact that near all research is done using different tools, techniques and parameters. In addition it is a translational field, requiring expert knowledge in both physics and biology. In order to accelerate this research, we aim to develop a low cost, easy-to-use tool, simplifying this transition between biology and physics.

Two devices were designed using three dimensional (3D) computer aided design (CAD) software, with a focus on being low cost, having a small footprint, portability and compatability with existing biological culture equipment. The devices were subsequently printed using 3D-printing technology, and assembled.

Thereafter, the essential part of calibrating the devices was performed in order to determine the performance of the device. Multiple characterization techniques were implemented in order to optimize the performance of the devices, as well as determining ultrasonic pressures. Electrical impedance scans and pulse-echo frequency sweeps were performed to find optimal operational frequencies. Pressure distribution was characterized using 3D free-field hydrophone scans. Power ramps were performed to correlate electrical power input to acoustic pressure output. To improve performance, transmission line transformers (TLT) were implemented as an electrical impedance matching network.

Lastly, to predict the complex interaction with the biological cell culture chambers, four dimensional (4D) simulations were performed.

Results showed that by following a strict fabrication protocol, the ultrasound transducers had a variance of $< 1\%$. The TLTs reduced the electrical reflection coefficient magnitude by a factor up to 2.9 and increased the acoustic power output by a factor of 3.15.

Simulations showed that when introducing complex interfaces as seen in cell culture chambers, multiple reflections were created. This resulted in destructive and constructive interference, making the ultrasound field "unpredictable".

In conclusion, it has been demonstrated that following the protocol described, it was possible to make reliable and reproducible devices that simplify *in vitro* ultrasound experiments. Nevertheless, the complex interactions with biological equipment have to be evaluated further.

Contents

Nomenclature

Roman Symbols

3D Three-dimensional
4D Four-dimensional
CAD Computer Aided Design
DB-25 D-subminiature 25
DNA Deoxyribonucleic acid
FEM Finite Element Method
FFT Fast Fourier Transform
FFT Fast Fourier Transform
FWHM Full Width Half Maximum
HIFU High-Intensity Focused Ultrasound
IEC International Electrotechnical Commission
IGDD Image Guided Drug Delivery
MFH Magnetic Fluid Hyperthermia
MI Mechanical Index
MRI Magnetic Resonance Imaging
NLR Non-linearity ratio
PVDF Polyvinylidene Fluoride
RF Radio Frequency
TI Thermal Index
TLT Transmission line transformer

Chapter 1

Introduction

1.1 Cancer

According to the World Health Organisation, cancer was amongst the leading causes of death, causing 8.2 million deaths [1]. At the current rate of population growth, it is projected that cancer incidences will increase from 14 million in 2012, to 22 million by 2032 [1]. Currently, cancer prevention, is achieved by vaccination [2–4] and controlling environmental factors, *e.g.,* smoking and exposure to asbestos. Although such methods will reduce cancer incidence it is not a viable option for eradicating cancer. This calls for an improvement in cancer treatment.

One of the major problems in cancer treatment is late stage diagnosis. This is a problem because current clinical treatment options are not sufficient for late stage cancers. Such treatment methods are used only to slightly improve the life span, or increase patient comfort, *i.e.*, palliative treatment [5].

Several methods proposed to establish an earlier diagnoses, such as self-examinations and screenings. However, screenings and self-examinations have shown to be ineffective for decreasing breast cancer mortality due to a high rate of false-positives [6, 7].

In order to understand the treatments of cancer, it is important to gain an insight into what cancer is, and how it occurs. The formation of cancerous cells occurs during a process called the cell divison cycle [8]. This is the process where a cell copies its own genetic code, the DNA, and create a replica of itself. This

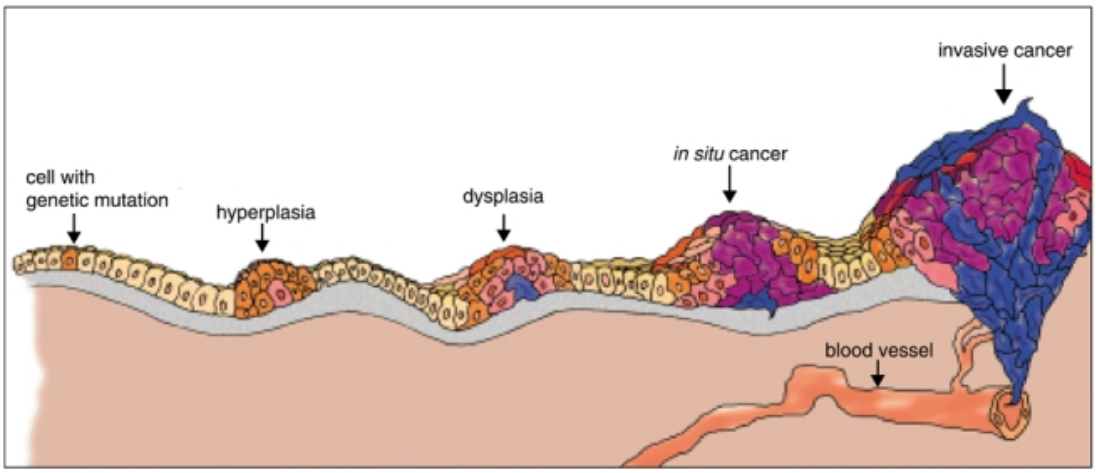

Figure 1.1: Schematic of the development of a cancerous tumor. The tumor is considered pre-cancerous until it is called an *in situ* cancer [9].

process is not always exact, and the newly created daughter cells might have a mutation. Normally, when a mutation occurs during the cell division cycle, the mutated cells performs apoptosis, programmed cell death, and no further growth of mutated cells occurs. However, the mutated cells might continue to reproduce, and passing on its mutated DNA to its daughter cells, which in turn produces another cell, and so on. The resulting collection of cells in a tissue which do not have the same function as their mother cells, is called a hyperplasia. All cancerous tumors start by this process, but are usually the result of multiple mutations [10]. In **Figure 1.1** the evolution of a cancerous tumor can be seen, and while it ends up as a cancerous tumor in this figure, this is not always the case. Often the development stops or stays dormant at any of the pre-cancerous stages [11].

When the tumor has developed into a cancerous stage, there are several factors that determine the mortality. Some of these factors are vascularisation, proliferation, location, metastasis, and the stage of the tumor. In **Figure 1.2** the survivability of a few cancer types are plotted, and as can be seen there is clearly a difference in the mortality of certain types of cancer.

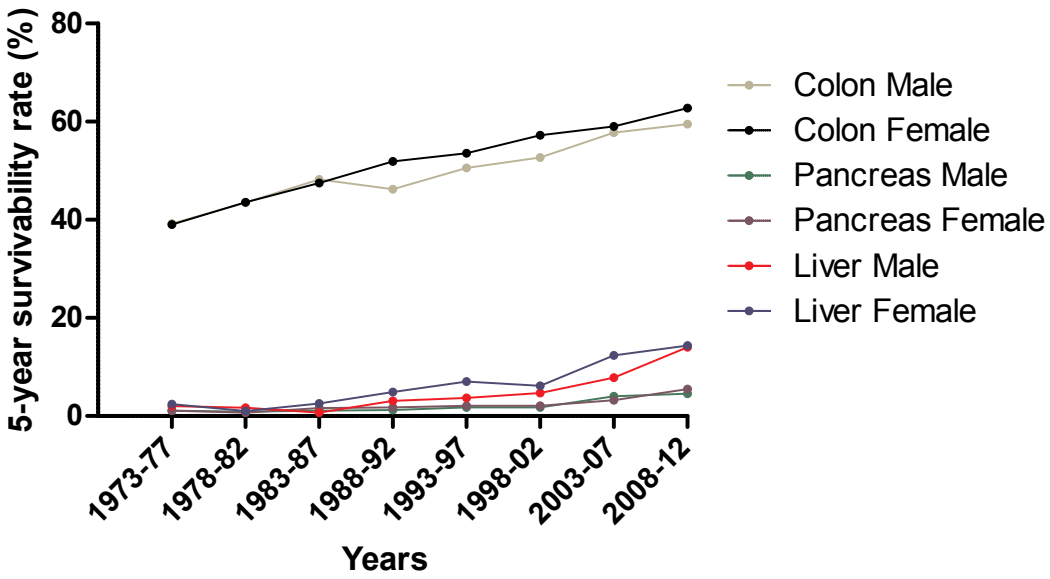

Figure 1.2: 5-year cancer survivability rate in percent for 3 different cancer types in males and females. [12]

1.2 Cancer treatment options

The aim of all cancer treatment methods is to kill and/or remove cancerous tissue while leaving the healthy tissue intact. The challenge here lies in the latter requirement, as there are a vast amount of ways to kill cells, but to only kill specific cells is more difficult. The three most common cancer treatments are surgery, chemotherapy, and radiotherapy [13]. They are either used in combination or by themselves. This is decided by an oncologist and is patient specific [13].

1.2.1 Clinically used treatment options

In many cases surgery is the only hope for a complete cure of cancerous tumors, as it might be possible to remove all cancerous tissue. However, surgery is not always possible to perform due to multiple factors. Surgery is not a possible option when the tumor is located at an inaccessible site, or the tumor is too developed with major veins encapsulating it, or the patient health does not allow invasive procedures [14].

Chemotherapy is another treatment option used in many cases. There are a vast magnitude of chemotherapeutics, most of which exploit a difference between normal tissue and cancerous tissue; the high proliferation rate of cancerous cells. This is done by in essence targeting all cells in the body which have a high rate of regeneration, by introducing chemicals which cause destructive damage to a cell during the cell division cycle. Unfortunately, not only cancerous cells are proliferating in the body, which causes the chemotherapeutics to destroy healthy cells as well, causing major side effects. Furthermore, making sure all the cancerous cells are exposed to the chemotherapeutics is of highest importance, and remains a problem with most chemotherapeutic agents [15].

Radiation therapy is a non-invasive treatment option that uses high energy electromagnetic radiation (photons) to kill cancerous cells by causing irreparable damage to vital parts of the cell [16]. There are two main mechanisms radiation therapy works; direct and indirect. The direct mechanism is when a photon is interacting with the nucleus of the cell, breaking the strands of the DNA causing destructive re-arrangements. The indirect mechanism is when a photon is interacting with the water in the cell lumen, creating free radicals which in turn causes damage to nearby structures inside the cell [17].

Although these three are the most commonly used, there are a lot of different experimental treatments that are being developed and gradually implemented into clinical use.

1.2.2 Experimental therapies

While all treatment modalities are constantly being researched, some have highly costumized experimental setups, and are not easily implementable to other hospitals. Particle therapy is similar to radiation therapy, but instead of radiating with high energy photons, particle therapy uses high energy atomic nuclei. The reason for this is a peculiar effect of particles traveling through tissue. Where the attenuation of photons in tissue is described mostly by an inverse exponential-function, the attenuation of a particle is more complex. When a stream of particles is traveling through the body, they gradually lose their energy, until a certain point. At this point almost all of the particle energy is absorbed, which

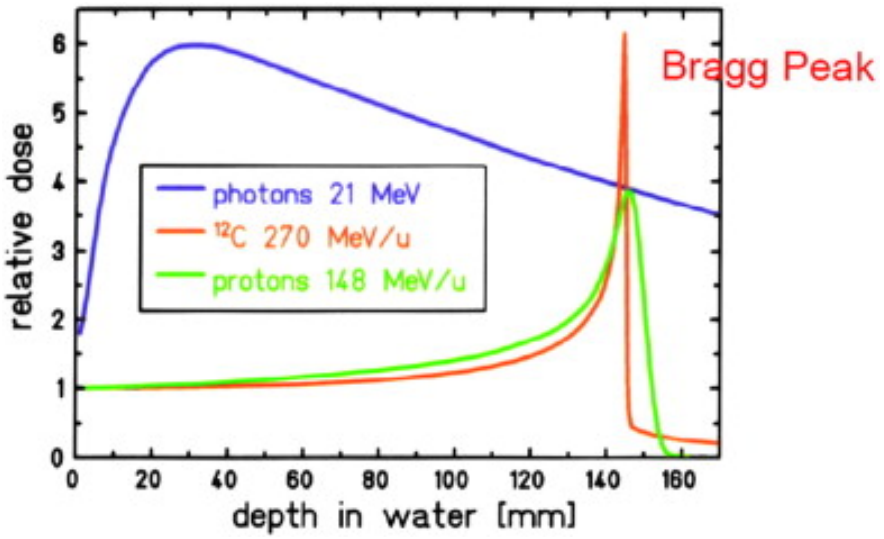

Figure 1.3: The relative dose deposited in water for high energy photons, protons and carbon-atoms. [18]

causes tissue damage in that region. This rise in relative dose at a certain depth in the ray-path is called the Bragg peak, as seen in **Figure 1.3**.

High-Intensity Focused Ultrasound (HIFU) utilizes the thermal heating effect of ultrasound in combination with the ability to focus the ultrasound to ablate tissue [19]. When cells reach a temperature between 50-60 °C they are instantaneously killed [20, 21]. In contrast to radiotherapy, which is also a non-invasive treatment modality, HIFU does not seem to damage tissue surrounding the focus at all [20]. This gives a great advantage to HIFU, making it possible to give multiple treatments whereas with radiotherapy this is usually not an option [20]. The high intensity ultrasound can also result in non-thermal effects, in particular a phenomenon called inertial cavitation, which is the spontaneous formation of bubbles in the ultrasound field due to the high negative pressure [20]. Inertial cavitation has been observed in some HIFU studies, and generally should be avoided, since it makes the lesions formed less predictable in shape and can thus damage healthy tissue situated close to the tissue that should be ablated [20]. This is solved by using intensities that are not high enough to produce inertial cavitation, but still high enough to produce a thermal effect, and rather sonicate for a longer duration [20].

Another modality that uses heat to kill cells is Magnetic Fluid Hyperthermia (MFH). Here Magnetic nano particles are injected directly into a tumor, and subsequently exposed to an alternating magnetic field. This causes the magnetic nano particles to try to align themselves with the magnetic field, and will then generate heat due to their movement. Magnetic nano particles have also been coated with specific proteins, causing them to attach to cells with a corresponding protein in their cell membrane. If this is a protein that identifies cancerous cells, the magnetic nano particles can be imaged in a Magnetic Resonance Imaging (MRI) machine. After observing with an MRI-scanner that all the magnetic nano particles are gathered at a tumor, MFH can be used to treat the tumor. This means that these MNPs can be used for both diagnostic and therapeutic purposes (theranostic) [22, 23]. MFH has been used to treat prostate cancer in humans clinical trials [24].

1.3 Sonoporation

Sonoporation is the transient formation of pores in cells, due to the application of ultrasound or ultrasound in combination with microbubbles. By focusing the ultrasound in a certain region, drug uptake can be locally increased. Several mechanisms for the increased drug uptake have been hypothesized [20, 25]. The possible mechanisms can be separated into two categories; thermal effects and mechanical effects [20, 25, 26]. The increased drug uptake caused by the thermal effect has been seen in other modalities, such as MFH [27]. It is hypothesized that the increased drug uptake is due to transient pores being created in the cellular wall [25]. There are several mechanisms that create these transient pores, recreated in **Figure 1.4** [25]. At lower ultrasound intensities there are mainly four possible mechanisms for the creation of transient pores. The push and pull effect are occurring in the two extremes of a bubble oscillation. The push effect occurs when a bubble is at its maximum radius in the proximity of a cell wall, pushing a hole in the lipid bilayer cell membrane. The pull effect occurs at the opposite phase of the bubble oscillation, when the bubble is at its smallest radius, and pulls surrounding liquid towards itself which can also cause pores. The translation effect happens when a bubble is at its minimum and gets pushed through the cell

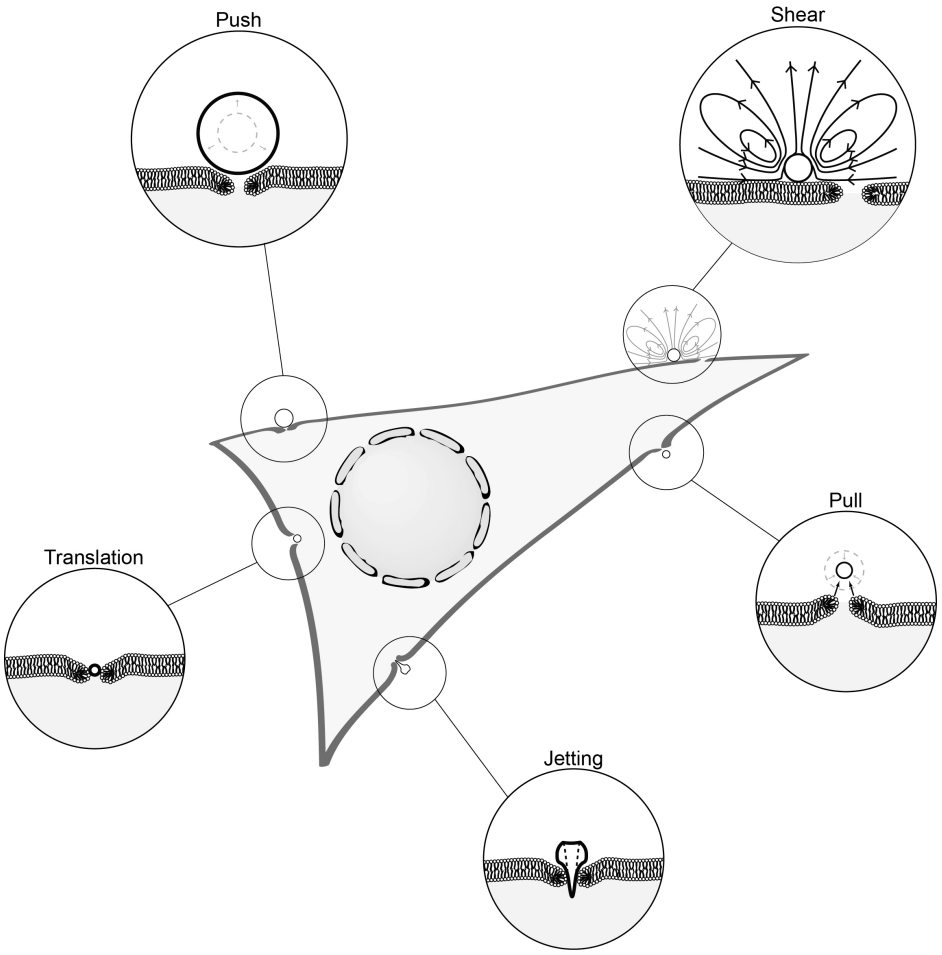

Figure 1.4: Mechanisms of sonoporation. The triangular shape is a cross section of a cell encapsulated with a lipid bilayer membrane with a nucleus in the center of the cell. The events around the cell wall are the physical mechanisms sonoporation. The small circles around the cell membrane are microbubbles [25].

wall, ending up on the inside of the cell. When the bubble is oscillating with a liquid surrounding it will push and pull on the liquid, causing streaming which in turn might shear open a cell wall [25, 26].

The size of the bubbles are $< 6\,\mu$m diameter and typical oscillations are at the magnitude of 2 MHz [28]. This calls for high magnification with microscopes and very high speed cameras in order to capture the bubble dynamics. These kind of experiments done with cells are done with only a single cell layer, and are not sufficient to determine any efficacy of drugs, merely mechanism [25, 29].

The dynamics of a bubble in an ultrasound field is a complicated field of study, as the behavior of the bubble is highly connected with the characteristics of the ultrasound field [28]. On the other hand, performing biological experiments on cells requires a specialized knowledge on cells and biochemistry. Thus the research of sonoporation requires an intricate knowledge of the physics of ultrasound in addition to an intricate knowledge of biology and biochemistry. In order for to perform high quality sonoporation experiments, all acoustic parameters of the experimental set up have to be known.

A benefit of using ultrasound to deliver drugs is that it can be used to image the diseased area at the same as treating it, also called image guided drug delivery (IGDD). Making this another modality that can be called theranostic.

1.3.1 Ongoing sonoporation research

The group for experimental acoustics at the Institute for Physics and Technology at the University of Bergen, to which the author is affiliated, is currently involved with a research project in sonoporation. The aim of this project is to improve and research the effect of sonoporation. Specifically, the project is aimed at the treatment of pancreatic adenocarcinoma with the help of sonoporation. This is a translational research project, which involves physicists, pharmacists, medical doctors and biologists. As such, a close cooperation is important between the different professionals allowing a limited cross field knowledge. The world first human trial on sonoporation as a treatment modality for pancreatic adenocarcinoma has already been done as a result of this project [30], but still the improvement of sonoporation conditions and evaluation of sonoporation for other uses still needs to be done.

1.4 Tools for *in vitro* sonoporation

A cornerstone of all scientific research is the replication of studies. With ultrasound research this presents a problem, as the sound field distribution changes with respect to probes used, and alignment of the setup. This places a high importance to the calibration of the ultrasound field of the probes, and the

medium the probes are used in.

A very superficial way of describing an *in vitro* sonoporation experiment is mixing cells with microbubbles into a container, and then exposing the mixture to ultrasound of different intensities. However, varying the intensity of the ultrasound might not be as trivial as one would guess. The ultrasound field is highly dependent on the medium in which it is propagating. Which leads to the importance of the alignment of the ultrasound source to the sample that is to be sonicated, and the acoustic properties of the container. The presence of inhomogenities in the medium of the ultrasound can produce reflections, and have different attenuation properties. This creates a high importance of knowing the ultrasonic behavior of everything that is in the sound field. The mechanisms of sonoporation seems to be correlated with the pressure amplitude of the ultrasound wave [25]. Hence, a precisely calibrated ultrasound field is paramount to correlate pressures with biological effects.

Several different experimental setups are being used for *in vitro* sonoporation experiments, using different containers designed for biological samples. There are several commercially available ultrasound systems available being designed for general ultrasound experiments and even sonoporation experiments, such as the Artison Sonitron 2000 [31] and Sonidel SP100 [32]. These are single element probes, calibrated by the manufacturer in free field conditions. The ultrasound field in front of a transducer is not uniform in any plane, and needs to be calibrated. This might not be optimal for all experimental setups, due to interference in the sound field caused by reflections from boundaries. Furthermore, the ultrasound probes used are required to be calibrated at all times, as they might suffer temporal degradation and are easily damaged. Hence, they ought to be frequently re-calibrated, which can be costly if performed at remote laboratories.

A very important challenge in the state-of-the-art ultrasound research is the control of the ultrasound parameters [33], accurately determining the pressure the samples are exposed to. This thesis will be on the development of characterized ultrasound tools designed to be used for *in vitro* experiments.

1.5 Requirements for treatment devices

In order to make the devices as efficient as possible, the design has to be considered from both a physicist and a cellular biologists prespective. As there are several different cell culture containers readily available in most laboratories, the devices should be designed around them, ensuring compatibility and familiarity. Furthermore, they should be easy to use, without the necessity of alignment or knowledge of ultrasonics. As laboratories often have a limited space, they ought to be made compact, allowing placement in cramped sterile chambers.

1.6 Objectives of thesis

This thesis will be about the development and acoustic characterisation of ultrasonic treatment tools, designed to perform experiments on *in vitro* cells, and is based on the authors peer reviewed publication [34].

1.7 Structure of thesis

This thesis is divided into 5 chapters.

In the next chapter some basic concepts within ultrasound are presented, such as the theory of propagation and acoustic material characterisation. A brief introduction to ultrasound in biology, and some of the units used to determine the effect the ultrasound has on biological tissue, is also introduced. As there are multiple different ways to investigate the ultrasound field, some of the measurement equipment and techniques are also discussed.

The third chapter describes the design and fabrication process of the proposed devices, including the characterizing of the ultrasound field. Furthermore, as the *in vitro* application is more difficult to evaluate physically, simulations were performed to evaluate the ultrasonic field.

In the fourth chapter, the results of all experiments and simulations are presented and discussed

In the fifth chapter, the conclusion of the thesis is presented.

Chapter 2

Ultrasound characterisation theory

2.1 Ultrasound

The definition of ultrasound is sound with frequency higher than $f = 20000\,\text{Hz}$. Sound is a propagating pressure wave which has one phase with a higher and one with a lower pressure than the equilibrium [35]. Sound waves needs a medium to propagate through, in contrast to electromagnetic waves, which can travel through vacuum as well. A simple monotone wave is illustrated in **Figure 2.1**, both in space and time. Some of the most important properties of a wave are also indicated in **Figure 2.1**, namely the frequency, f, wavelength, λ, and the speed of sound, c which are all related by the equation:

$$c = \lambda f \tag{2.1}$$

The linearised continuity equation states that the inflow of mass into a volume must equal the mass a volume gains [35]:

$$\rho_0 \frac{\partial s}{\partial t} + \boldsymbol{\nabla} \cdot (\rho_0 \mathbf{v}) = 0, \tag{2.2}$$

where ρ_0 is the equilibrium density, $s = \frac{\rho - \rho_0}{\rho_0}$ is the condensation, $\mathbf{v} = \mathbf{v}(t)$ is the instantaneous particle velocity. This can be combined with the linear Euler's

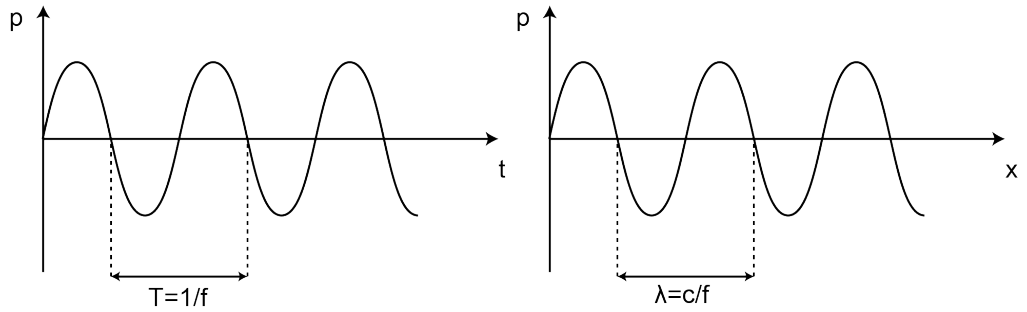

Figure 2.1: A simple sound wave in time and space, where the vertical axis represents the pressure in both graphs. The left graph displays the pressure in a single point observed from a traveling wave in the time domain. The right graph shows how a wave would be distributed in space at a certain time.

equation, which is a fluid version of Newton's second law [35]:

$$\rho_0 \frac{\partial \mathbf{v}}{\partial t} = -\boldsymbol{\nabla} p, \tag{2.3}$$

where p is the acoustic pressure. This yields:

$$\boldsymbol{\nabla}^2 p = \rho_0 \frac{\partial^2 s}{\partial t^2} \tag{2.4}$$

In order to make **Equation 2.4** into a differential equation of one variable, a relation between the pressure and the condensation is needed. Here we use [36]:

$$p = P - P_0 = As + \frac{Bs^2}{2} + \cdots, \tag{2.5}$$

where P is the absolute pressure, P_0 is the ambient pressure, and A and B are constants. This comes from a taylor expansion around ρ_0 and for small values of s. **Equation 2.5** can be approximated by disregarding all higher order terms, which inserted into **Equation 2.4** gives:

$$\boldsymbol{\nabla}^2 p = \frac{\rho_0}{A} \frac{\partial^2 p}{\partial t^2} = \frac{1}{c^2} \frac{\partial^2 p}{\partial t^2}, \tag{2.6}$$

which is the lossless, linear wave equation. The solution to this equation for a

plane wave is [35]:

$$p = P_1 e^{i(\omega t - \mathbf{k}\cdot\mathbf{r})} + P_2 e^{i(\omega t + \mathbf{k}\cdot\mathbf{r})}, \tag{2.7}$$

where the propagation vector $\mathbf{k} = k_x\mathbf{i} + k_y\mathbf{j} + k_z\mathbf{k}$ is introduced, and $\omega = 2\pi f$ is the angular frequency. The propagation vector is defined by $|k| = \frac{\omega}{c}$, from insertion into **eq. 2.6**.

2.1.1 Acoustic impedance

The acoustic impedance is an analogue to the electric impedance, where the electric impedance is defined by the ratio of voltage to current. Acoustic impedance is defined by the instantaneous pressure divided by the instantaneous particle velocity, and for a spherical wave in a lossless medium it is [36]:

$$Z_A = \frac{p}{\mathbf{v}} = \rho_0 c \left(1 + 1\frac{A}{r}\right), \tag{2.8}$$

where $p = p(t)$ is the instantaneous pressure, ρ_0 is the equilibrium density, r is the distance from the source of the wave at the origin of the coordinate system. Far away from the source or for plane waves the specific acoustic impedance takes a value called the characteristic impedance, which is a property of the medium only [36]:

$$z = \lim_{r\to\infty} Z_A = \rho_0 c. \tag{2.9}$$

Thus, two of the most important parameters for an ultrasound medium is the speed of sound, c, and the equilibrium density, ρ_0, and the measurement of these will be discussed later in **Section 2.5.3**.

2.1.2 Nonlinear propagation

The linear pressure wave equation makes a very important assumption when relating the condensation to the acoustic pressure in **Equation 2.4**. For nonlinear pressure waves the second order term is also taken into account, and thus not only the constant A needs to be determined. The ratio $\frac{B}{2A}$ is known as the nonlinearity constant, and the larger it is, the more nonlinearly the medium behaves. At high pressures, an acoustic wave gets distorted as it is traveling, which can be observed

in many ways. The simplest way is by direct inspection of the wave, seeing if it appears to have any differences from a normal sine wave. A very easy indicator in the time domain is to look at the peak positive and the peak negative pressures, where a peak positive pressure value larger than the peak negative pressure value indicates a nonlinear wave. The ratio of the peak positive (p_{pp}) and peak negative (p_{pn}) pressure:

$$\text{NLR} = \frac{p_{pp}}{p_{pn}} + 1, \tag{2.10}$$

provides an easy to calculate indication of the nonlinearity of the ultrasound signal and is called the nonlinearity-ratio (NLR). As the NLR increases the more nonlinear the wave. This effect can also be seen in the frequency domain with the help of a fast fourier transform (FFT) of the signal. In an FFT nonlinearty is detected by detecting peaks of higher harmonics in the ultrasound signal. This can be explained by the transfer of energy into higher frequency harmonics [36]. In a lossless liquid, this effect can transform a traveling wave into a perfect saw-tooth wave after a fixed length, x_s [28]:

$$x_s = \frac{\pi c^2}{2v_0\omega(1 + \frac{B}{2A})}, \tag{2.11}$$

where v_0 is the amplitude of the particle velocity $\mathbf{v}$, $\omega = 2\pi f$ is the angular frequency. Although in a real liquid this could not happen due to the frequency dependent attenuation, with increasing attenuation at increasing frequencies.

nonlinearity can also occur from the transducer itself, due to nonlinear vibration of the surface or nonlinearity in the driving circuit of the transducer.

2.2 Ultrasound transducers

A transducer is a device that transform one form of energy to another. Ultrasound is made and observed using ultrasound transducers, usually just referred to as transducers. There are also specialized listening transducers, which are called hydrophones or microphones, when used in water and air respectively. A hydrophone is a very important tool for calibrating sound fields, and will be discussed more in **Section 2.4**.

Ultrasound is used in a vast amount of applications, and usually the transducers has to be constructed for a specific purpose [37]. There are many different type of basic transducer designs, but the most popular currently used in medical ultrasound is based on piezoelectric materials [38]. Piezoelectric materials are non-conductive materials which have an asymmetrical charge distribution. The simplest piezoelectric transducers consist of a single piezoelectric material which is covered by an electrode on two surfaces with a coax cable connected to the electrodes [37].

The construction of a transducer determines what the transducer can be used for. Transducers used for imaging, and detecting need to have a high temporal resolution. This is achieved by making them broadband, which means they have an increased sensitivity for frequencies around the center frequency, compared to a narrowband transducer.

The center frequency is defined [39]:

$$f_c = f_l + \frac{f_u - f_l}{2}, \tag{2.12}$$

where f_c is the center frequency, f_l is the lower and f_u is the upper frequency limit. The lower and upper frequency limits are the frequencies where the acoustic output from the transducers are reduced by a certain limit. Often this limit is given in dB reduction from the highest acoustic output. Using the same f_l and f_u, the bandwidth, BW, can be calculated using [39]:

$$\mathrm{BW} = f_l - f_u \tag{2.13}$$

The percentage bandwidth, %BW, and mechanical quality factor, Q_m, can be calculated with:

$$\%\mathrm{BW} = 100\frac{\mathrm{BW}}{f_c}, \tag{2.14}$$

and

$$Q_m = \frac{f_c}{\mathrm{BW}}. \tag{2.15}$$

A schematic for a basic transducer design can be seen in **Fig. 3.2**, where a backing layer is visible behind the active piezoelectric element. Although the

backing layer is not in contact with the medium the ultrasound is propagating in, it plays an important in the transducer performance. With a heavy backing, the transducer gets a wider bandwidth, lower maximum output at resonance, and it will ring less after excitation. Conversely with a light backing it will get a narrow bandwidth, high maximum output at resonance, and it will ring comparatively more after excitation.

2.2.1 Sound field

Typically the sound field from an ultrasound transducer is divided into two sections; the near field and the far field [40]. The near field is closest to the transducer, and is characterized by an interference pattern with constructive and destructive interference. The far field is usually defined to start where the last maximum in the interference pattern from the near field.

The shape and characteristics of the acoustic pressure distribution made by an ultrasound transducer is dependent on the geometrical specifications of the transducer, the frequency and the medium in which the wave is propagating. The resulting ultrasound field from the transducer can be modeled with analytic mathematics using several simplifications. Although these models might give a good estimation of how the physical transducer might behave and emit sound, due to several of the assumptions and simplifications, they are not sufficient.

In order to solve this problem, several numerical methods have been developed, such as the Finite Element Method (FEM) [41]. This method is used for several types of engineering and physics tasks, such as construction evaluation, aerodynamics computations and of course sound and ultrasound. The FEM works by subdividing the physical quantities in small elements, and solving the partial differential equations which describes the ultrasound propagation.

A circular transducer is one of the simplest cases to consider and it can be modeled analytically by considering it to be a piston moving forwards and backwards in an infinite medium, and surrounded by an infinite and rigid baffle. Furthermore, the sound field created by a circular transducer is circularly symmetrical, which allows mathematical simplification. Several important factors are found by this derivation which is done many places [35]. One is the near field

distance N_d which is the axial distance from the center of the transducer to the point in the ultrasound field where usually the highest pressure is found:

$$N_d = \frac{a^2}{\lambda}, \tag{2.16}$$

where a is the radius of the oscillating surface, and λ is the wavelength in the medium in which the pressure wave is propagating.

2.2.2 Electric impedance characterisation and matching

A lot of the acoustic behaviour can be determined by the electric impedance of a transducer, such as the acoustic resonance frequency [42]. The electric impedance,Z_E is defined as [43]:

$$Z_E = \frac{V}{I}, \tag{2.17}$$

where V is the instantanous voltage, and I is the instantaneous current. The electric impedance of a piezoelectric material is generally a complex value which changes with frequency, and it can be measured over several frequencies with an impedance analyzer. An impedance analyser works by sending out a mono-frequency pulse into an electrical network, then "listening" to the pulse received back at the same port. Comparing the output pulse, to the received pulse, the electrical impedance Z_E can be calculated [44]. From a frequency sweep, characteristic relative changes in the impedance reveals the resonance frequencies of the piezoelectric material.

However, the electric impedance at the resonance frequency is not necessarily matched to a typical driving source. In order to deliver the maximum amount of power from a driving source to a circuit, the circuit needs to be electrically impedance matched to the driving source. To be electrically impedance matched means that the driving circuit is the complex conjugate of the impedance of the source:

$$Z_{E,s} = Z^*_{E,c}, \tag{2.18}$$

where $Z_{E,s}$ is the source impedance and $Z_{E,c}$ is the circuit impedance, and the

* represents the complex conjugate. Ultrasound radio frequency (RF) amplifiers usually have a source impedance of $Z_{E,s} = 50 + i0\,\Omega$. Thus, in order to maximize power transfer to the transducer circuit, the circuit impedance needs to be $Z_{E,c} = 50\,\Omega$. This can be ameliorated by building matching networks to the transducer, which alters the impedance of the circuit. A helpful value to evaluate how well matched to $50\,\Omega$ is the electrical reflection coefficient magnitude:

$$\delta = \sqrt{\left(\frac{R^2 - Z_{E,c}^2 + X^2}{(R^2 + Z_{E,c})^2 + X^2}\right)^2 + \left(\frac{2Z_{E,c}X}{(R + Z_{E,c})^2 + X^2}\right)^2}, \tag{2.19}$$

where R and X is the resistance and reactance of the circuit respectively. The reflection coefficient, δ, is 0 for 0% reflection, and 1 for 100% reflection. As the reflection coefficient magnitude takes into account the resistance and the reactance of the transducer, considering the reflection coefficient gives a quick indication of how a transducer would perform in a circuit.

Transmission line transformers (TLTs) are very popular electrical impedance matching components for antennas [45], and lately have been found to be a great resource for ultrasonic transducers as well [28]. TLTs work as voltage and impedance transformers, whilst keeping the power delivered to the circuit constant. Hence, while they are changing the voltage, they will also, by ohm's law, have to change the impedance of the circuit. The displacement of piezoelectric materials is dependent on the electric field set up throughout the material [37], and therefore the voltage [46]. Thus, when reducing the impedance, and therefore the voltage with a TLT, special care needs to be taken, as performing a perfect electrical impedance match might reduce the voltage, counteracting the benefits of the impedance matching.

2.3 Ultrasound in biology

Ultrasound has two main effects on tissue which can be destructive; thermal and mechanical effects. The thermal effect is due to the absorption of ultrasound in tissue, causing a temperature increase. In order to control the thermal exposure

of tissue a thermal index (TI) has been proposed [20]:

$$\mathrm{TI} = \frac{P}{P_{\mathrm{deg}}}, \tag{2.20}$$

where P is the transmitted acoustic power and P_{deg} is a tissue dependent and estimated value in order to heat the tissue by 1 °C. However this can not be used to represent actual *in vivo* temperature rise [20, 28]. Neither does it account for the exposure time, which also affects the accumulated temperature increase [20].

The mechanical effect is mainly due to the creation of inertial cavitation [28]. The mechanical index (M) is designed to be an indicator of the mechanical effects on the tissue [20, 28]:

$$\mathrm{MI} = \frac{p_{pn}}{\sqrt{f}}, \tag{2.21}$$

where f is the frequency in MHz, and p_{pn} is the pressure in MPa, but the MI is normalized to 1 MPa $\mathrm{MHz}^{-1/2}$. The higher the MI the higher the risk for tissue damage. This is due to the negative pressure which gives an increased risk of cavitation, and with lower frequencies comes larger wavelengths, which means a larger area of low pressure, also causing a higher risk of cavitation.

Many manufacturers supply information about intensity on their ultrasound products, however there are several ways of calculating the intensity, and these are not always given.

2.4 Ultrasound characterisation tools

Multiple methods exist to gain knowledge of the ultrasound field. Several considerations needs to be taken into account when choosing the right tool for measuring a specific sound field.

2.4.1 Hydrophones

Hydrophones are among the most important tools in most ultrasound labs, and they come in many different varieties. The different kinds of hydrophones have different areas of usage, depending on the characteristics of the sound field.

As hydrophones are placed into the sound field, it is important to take into consideration what influence they have on the sound field they are measuring.

Needle hydrophone A needle hydrophone gets its name from its shape, and a rough sketch of one can be seen in **Fig. 3.3**. The sensing element of a needle hydrophone is a small piezoelectric element (usually $< 1\,\text{mm}$ in diameter), located at the tip [36]. Inherently, there is a trade off between the spatial resolution and the sensitivity, due to the force dependence on the piezoelectric material. Needle hydrophones are designed in order to minimize reflections in the direction of the sound field. This allows them to be used close to transducers surfaces, without causing standing waves between the hydrophone and the transducer surface. However, care needs to be taken when doing high power measurements, in order to avoid hydrophone damage by cavitation. Furthermore, a needle hydrophone is fragile and extra care has to be taken when handling it.

Membrane hydrophone A membrane hydrophone is constructed by a thin unpoled polyvinylidene fluroide (PVDF) sheet, which is stretched over a ring [36]. An electrode is sputtered onto each side of the sheet, only overlapping in a small region which is then poled to become the active area [36]. Furthermore, using this technique with multiple electrodes, an array of sensing elements can be made. This allows for a 2 dimensional representation of at least a part of the sound field, depending on the size of the hydrophone and the sound field. The PVDF membrane has an increasing reflection coefficient with higher frequencies, which should be taken into account when measuring close to the transducer.

Fiber optic hydrophone The fiber optic hydrophone takes advantage of the changes of the optical refracitve index due to pressure changes. They are very robust compared to needle and membrane hydrophones.

2.4.2 Radiation force balance

Radiation force balances works by measuring the radiation force exerted by the ultrasound. This method does not reveal the pressure intensities in the field, but the total power exerted. A typical setup consists of placing a transducer in front

of a target, and measuring the force exerted on the target with a high precision scale. If the target is an absorbing target, the acoustic power of the transducer can be calculated with [36]:

$$P = cF = cmg, \tag{2.22}$$

where c is the speed of sound, F is the radiation force, m is the measured "mass" of the radiation force, and g is the gravitational constant.

2.5 Characterisation standards

There are two main types of calibration methods for ultrasound transducers; primary and secondary. Primary means that the calibration method does not rely on previously calibrated ultrasound transducers, and it is often more intricate than the secondary methods. The secondary methods rely on a calibrated reference which is compared to the transducer to be calibrated.

2.5.1 Ultrasound field measurement standards

Primary calibrations are usually performed at national measurement laboratories, such as the National Physical Laboratory in the UK. Here high precision primary calibration techniques are used to make reference calibration tools, which in turn are used to calibrate consumer devices, such as hydrophones. The most known standard for ultrasound field measurements is the one made by the International Electrotechnical Commission (IEC). Several factors are stated by the IEC, which are of high importance to the precision of the ultrasound characterisation, such as the requirements of a setup [47].

Most secondary calibration methods of transducers have a setup with a transducer and a hydrophone in a water tank. The water in the tank has to be degassed and deionized in order to satisfy the conditions of [47]. This is both in order to increase the precision of the measurements, and to prevent inertial cavitation during high amplitude measurements, which can damage the hydrophone.

2.5.2 Field scan calibration

Typically this is done inside a water tank, where a hydrophone is moved around in the sound field of a transducer, noting down the pressure value of each point [48]. The hydrophone is usually calibrated in a water tank with a temperature of 20 °C, and thus the water in which the hydrophone is used to calibrate a transducer need to be the same temperature.

2.5.3 Material characterisation

Measuring the acoustic properties of materials is very important for transducer construction, as the material parameters of each component in the transducer affects the performance of the transducer. By knowing the characteristic acoustic impedance, z, and the attenuation coefficient, α, of a material, most of its acoustic behavior can be predicted. Thus the speed of sound, c, the volume V, the weight, m, have to be measured in order to calculate z, while α can be measured directly. If the samples are constructed with a simple geometry (*e.g.* a disc) the measurement of the volume and weight is rather straight forward, but the speed of sound c has to be measured acoustically. Measuring the speed of sound can be done with several techniques, in the time and frequency domain. The simplest method is the insertion technique, measured in the time domain. Here two measurements are done, with two transducers, or one transducer and one hydrophone. The first measurement is measuring the time it takes for an ultrasound wave to travel from one transducer to the other with just water between them. The second measurement is done with the two transducers in the same place, with the sample inserted between them. Using the thickness measurement done in the volume measurement, the speed of sound can be calculated with [49, 50]:

$$c_p = \frac{d_s}{t_2 - t_1 + \frac{d_s}{c_w}}, \tag{2.23}$$

where c_p is the compressional speed of sound, d_s is the thickness of the sample to be characterized, t_1 is the transit time without a sample inserted, t_2 is the transit time with the sample inserted, and c_w is the speed of sound in water.

In distilled water, an emperical equation estimating the speed of sound, c_w,

accurate to within 0.05% is [35]:

$$c_w = (1.4027 + 48.8T - 48.2T^2 + 13.5T^3 + P_G(15.9 + 280T + 240T^2)) \cdot 10^3, \quad (2.24)$$

where T is temperature in degrees Celsius, and P_G is gauge pressure in Pascal. This equation is accurate to within 0.05% for $0 < T100\,^{\circ}\mathrm{C}$ and $0 \leq P_G \leq 20\,\mathrm{MPa}$. From the same measurements the attenuation can be measured, by comparing the waveform with and without the sample inserted. The attenuation coefficient is a combination of the scattering and absorption of the travelling wave, and these can not be separated using this technique.

Chapter 3

Materials and methods

3.1 The chamber

The devices were constructed for two different experimental setups; one primarily for cells floating in a culture medium and the other for adherent cells. Device A was designed for a floating cell setup and based on a 24-well plate; a commonly used perspex plate with 24 separated circular wells. Device B was designed for an adherent cell setup and based on a closed chamber design with optically clear walls, such as an OptiCell^{TM} or PetakaG3^{TM}. An OptiCell^{TM} is a 10 mL chamber with 100 μm thick transparent walls, and can be seen in **Figure 3.1C**. The PetakaG3^{TM} is a very similar construction, but with a larger volume and 200 μm thick walls; in addition it allows for controlled oxygen saturation *i.e.* a bioreactor. These cell culture devices were chosen as they are completely submersible and allow ultrasound propagation through the entire device. In order to increase versatility, the sonication chambers were designed in 2 or 3 parts; a base plate, an extension frame, and depending on the requirement, a carriage frame. This was done in order to make the devices as modular as possible, allowing quick and non-destructive modifications, as well as enabling free-field characterization. The base plate was designed with 6 circular sockets each fitting an ultrasound transducer. In addition, they were designed with a rectangular slot in one of the narrow sides of the base plate (*cf.* **Fig. 3.1A,C**), allowing insertion of an electrical connection interface. The extension frame was designed with hollow

walls, allowing a reduction in material quantity and therefore cost, in addition to making the construction lighter. The carriage frame was designed to place the OptiCell™ or PetakaG3™ into the center of acoustic foci from the transducers. Six transducers were chosen as this allows the sonication of multiple samples simultaneously, which increases experimental throughput and statistical power. Both devices were also designed to be compact, in order to fit into cramped sterile environments. Surfaces that do not contribute to the functionality of the devices were designed to be curved, to increase structural integrity, ease of handling and aesthetics.

In device A the height of the extension frame and placement of the sockets in the base plate ensured that the acoustic foci are exactly in the center of the wells as illustrated in **Figure 3.1A-B**. In addition, the sockets were placed such that they were as far away from each other as possible to reduce interference between them, while still not too close to the wall causing reflections. The device was designed to place the 24-well plate inverted, as the bottom of the 24-well plate is very thick, which causes significant acoustic losses inside the wells. The top of the plate was covered with a self-adhering thin membrane (TopSeal™-A 24,Perkin Elmer, Waltham, MA), ensuring no leakage from the wells into the water bath. Alignment tabs ensured that the 24-well plate would only fit onto the extension frame in a single perfect way, guaranteeing optimal alignment each and every time.

In device B the transducer sockets were placed closer together, in order to restrict the ultrasound to the cell culture surface of the OptiCell™ and PetakaG3™, as illustrated in **Figure 3.1C-D**. Furthermore, the extension frame in device B was made significantly larger, as this would allow the ultrasound to propagate further. This will minimize distortions of the ultrasound field in the culture devices, caused by the reflections from the water/air interface. By using an OptiCell™ the same cell culture can be treated simultaneously, with 6 main areas of treatment. After treatment the membrane can be cut, allowing samples to be evaluated separately, using different methods.

The chambers had to be made of materials which are waterproof and water resistant, and preferably an electrical isolating material. A 3D-printer was chosen to make the base plate, extension frame, and the carriage frame. 3D-printer

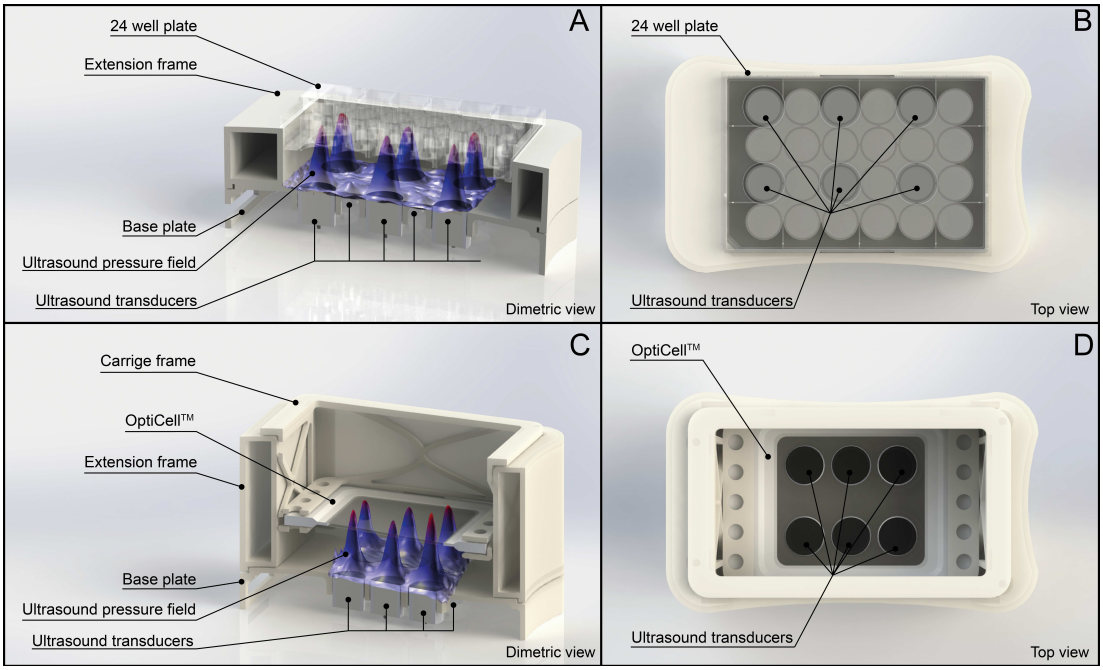

Figure 3.1: Computer generated renderings of prototype devices. Cutaway diagram showing assembly of ultrasound sonicators for 24-well plates (A and B) and OptiCells$^{\text{TM}}$ or PetakaG3$^{\text{TM}}$ (C and D) including the acoustic pressure fields. (B and D) Top view and position of the ultrasound transducers for both devices. In the OptiCell$^{\text{TM}}$ or PetakaG3$^{\text{TM}}$ sonicator, the ultrasound transducers have been places substantially closer.

technology allows manufacture of complex designs on demand and at a low cost. The 3D-printer used was a ProJet 1500 (3D Systems, Rock Hill, SC) capable of high resolution printing with $33 \times 25\,\mu$m in the xy plane, with a minimum layer thickness of $102\,\mu$m in the z-direction. All devices were designed in SolidWorks 2013 (Dassault Syst‘emes SolidWorks Corp., Waltham, MA).

3.1.1 Printing and post processing

Initial printer set-up takes approximately $15 - 30\,$min to check the correct orientation and support location. It was paramount to orientate the component correctly so the printing support structures were not placed on critical surfaces, *e.g.*, transducer sockets or inner walls. To prevent warping of the soft uncured 3D-printing material, the printing orientation was done such that only small

surfaces were being printed at any given time. The printer required about $5 - 8$ hours to finish each component. Once the 3D print was complete, 30 min of post processing, cleaning, and final curing of the frame components was required. A further 30 min was required to safely break the supports away and sand the surface. Sanding was performed in two steps. First with a mechanical sander to remove large artifacts left from the support (MS800B, Black & Decker, New Britain, CT). Following wet sanding (P180, 3M, St. Paul, MN) to smoothen the surfaces.

3.2 Ultrasound transducers

Each device required 6 transducers to be inserted into the bottom plate. The 6 transducers for each device were manufactured simultaneously in order to minimize differences between them. A summary of the assembly protocol for these transducers described in [51] is reproduced here. The transducer constituents can be seen in **Figure 3.2**.

The transducers were produced by attaching the positive pole of a ⌀15 mm, 2 mm thick PZ26 Navy Type I, lead zirconate titanate (PZT) disc to the inner core of a RG178/U coaxial cable using a conductive silver-loaded epoxy (Oxford

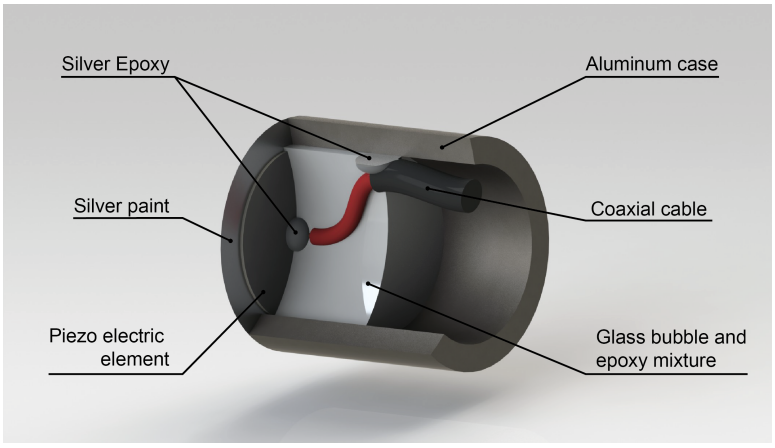

Figure 3.2: Cutaway diagram showing components and assembly of the ultrasound transducers. The front face of the transducer is connected to the earth via the case. This ensures a smooth surface with no electrodes. A low-density glass bubble and epoxy mixture has been used as backing to support the piezo with minimal damping.

Instruments, Abingdon, UK). The transducers were chosen to have a resonance frequency of 1 MHz, due to the wide usage of this frequency for therapeutic purposes and high availability of piezoelectric disks of this type. Furthermore, this relatively low frequency allows a high tissue penetration depth, making results easier to translate to *in vivo* studies. In order to have a resonance at 1 MHz the thickness of the disk had to be:

$$\frac{N_{\mathrm{t}}[\mathrm{mHz}^{-1}]}{f_{\mathrm{res}}[\mathrm{Hz}]} = \frac{2038}{1 \cdot 10^{6}} \approx 2\,\mathrm{mm\ thick},$$

where N_{t} is the thickness mode resonance frequency constant for PZ26, and f_{res} is the resonance frequency desired. PZ26 was chosen due to its high mechanical quality factor ($Q_{\mathrm{m}} > 1000$) and high piezoelectric charge coefficient ($d_{33} = 3.28 \cdot 10^{-10}\mathrm{CN}^{-1}$). This allows high acoustic amplitudes with minimal electrical power requirements, which grants the possibility to perform experiments at any desired acoustic amplitude. Moreover, PZ26 is a very durable piezoelectric material, with very low temporal degradation [52], which allows less frequent recalibration. The RG178/U coaxial cable was chosen due to its electrical shielding and its characteristic electrical impedance of 50 Ω, matching the characteristic impedance of the driving network. Furthermore, all transducers were fabricated with equal length cables, to ensure similarity. Silver epoxy was used instead of solder due to its adherent strength and flexible usage at low temperatures compared to solder. As solder requires localized high temperatures of up to 400 °C, this surpasses the Curie temperature of 330 °C for PZ26 [53, 54]. The conductivity of silver loaded epoxy increases until a saturation point when it is cured at temperatures up to 100 °C [55]. However, from previous experience curing the silver loaded epoxy onto PZ26, electrical discharges were observed when curing at temperatures over 80 °C. Whether this was due to the pyroelectric effect, or depoling was not investigated. Hence, a curing temperature of 80 °C was used, with a high precision oven (MINO/6, Genlab, Cheshire, United Kingdom). With this temperature sensitivity of the PZT, it is essential that the oven is of high precision and accuracy is used. The oven used has a listed temperature fluctuation of ±0.75 °C, and guided by a thermometer allowed curing at a temperature of 80 ± 0.75 °C as the thermometer uncertainty is less than 0.75 °C.

The next step was connecting the shielding of the coaxial cable to the aluminium case. This was also done with silver epoxy, as soldering to aluminium is highly challenging and requires temperature that can cause damage to the cable insulation. Aluminium was chosen because of its resistance to corrosion, as it will be exposed to water over long periods of time. In addition the case material has to be highly conductive, as it will be used to connect the front electrode of the PZT to the shielding of the coaxial cable.

The next step was to affix the PZT-disk to the case, which was done by placing the PZT and the case aligned concentrically on top of an adhesive ultra violet (UV)-tape (Adwill D-210, Lintec of America, Inc., Phoenix, AZ), and subsequently pour a mixture of EpoFix epoxy (Struers, Ballerup, Denmark) and K1 glass bubbles (3M) to fill up the entire aluminium cylinder. After the backing material was poured in, the transducers were put in a vacuum chamber where pressure was reduced to 0.5 mBar, thereafter rapidly increased to atmospheric pressure again. This ensured that the air bubbles trapped inside the mixture would expand, and rise to the top, when the pressure was increased again, they would burst. This alternating pressure cycle was done approximately 20 times, until no more air bubbles could be seen coming out of the backing material. The epoxy-glass bubble mixture was prepared as described in **Section 3.3**, with a glass bubble to epoxy weight ratio of 8-9:1, respectively. UV-tape was used because of its ease of removal following UV-light exposure. When removed this guaranteed a smooth surface on the entire front face of the transducer.

Subsequently the transducers were finished by applying a thin layer of silver paint on the front face, connecting the shielding layer of the coaxial cable to the front of the element, via the aluminium case. Applying the electrode like this minimizes the distortion of the surface. As a result this reduces the distortion of the sound field.

Dimensions	ID [mm]	OD [mm]	H [mm]
Case	17	25	25
PZT-disc	-	15	2

Table 3.1: Dimensions for transducer construction. ID - Inner diameter, OD - Outer diameter, H - Height

Table 3.1 shows the dimensions of the constituents of the transducers. The case was made significantly higher than the PZT-disc, in order to fill them up with sufficient backing material and to easily align the transducers into the sockets of the treatment devices.

3.2.1 Electrical impedance matching

After the transducers were built, electrical impedance scans were performed with a TE1000 impedance analyser (TrewMac, Adelaide, Australia). The scans performed were linear sweeps from 0.5 MHz to 5 MHz with 1000 samples, yielding a step size of 4.5 kHz. From the impedance, the reflection coefficient magnitude, δ, was calculated using **Equation 2.19**.

The thickness mode resonance frequency for the PZ26 disks used was:

$$f_{\text{res}}[\text{Hz}] = \frac{N_{\text{t}}[\text{mHz}^{-1}]}{d_{\text{PZT}}}\text{m} = \frac{2038}{0.002} = 1.0190\,\text{MHz}.$$

A matching network was then built using the electrical impedance magnitude, $|I|$, at the frequency with the lowest reflection coefficient magnitude, as this correlated with the thickness mode resonance frequency at ~ 1 MHz. This was done as all the transducers had a slightly different electrical impedance profile. The matching network made was to transform the electrical impedance to match the RF power amplifier source impedance of $Z_{\text{E,s}} = 50\,\Omega$. Transmission line transformers were used as the matching component in the matching network, due to their high power capabilities and low losses [56]. Furthermore, detailed descriptions of how to make multiple types of TLTs are available [57], with many different transformation ratios, making it trivial to find the right construction for most transducer impedance values. The TLTs were based on 12.5-mm-OD, 8.0-mm-ID, 6.5-mm-tall ferrite toroids (Amidon Associates, Costa Mesa, CA) and 28-AWG, 7-core wire with 250-μm insulation. Toroidal shaped ferrite cores were used, due to their constructional stability and ease of manufacturing. In order to prevent the cables from moving and potentially changing the characteristics of the transformer, they were glued in place (Loctite, Düsseldorf, Germany) onto the toroid.

When the TLTs were connected to the transducers, connectors had to be attached, compatible with a coaxial based driving system. As one of the main focuses when building these devices was ease of use, a non-conventional connector scheme was chosen, as this allowed a single plug for all 6 transducers. The connector scheme was based on a D-subminiature 25 (DB-25) connector. DB-25 was chosen as the connector due to the placement of the female connector in the device. When the female connector was placed inside the open slot in the base plate, as visible in **Figure 4.3**, the pins facing downward towards the transducers were inaccessible to the soldering iron. Hence, a connector with a sufficient amount of available connector pins when installed in the case was chosen. With a DB-25 connector, it was possible to only use the top row of the connector for all the transducers. The connection schematics used can be seen in **Figure 4.4C**. The ground of all the transducers was interconnected and connected to the outmost pins on both sides of the connector.

Two male connectors were made, one with a single coaxial cable with the innermost core connected to all of the active pins, and the shielding connected to both the ground pins. The second connector was made with 6 RG178/U coaxial cables with one BNC-connector each, with the innermost core connected to a pin each, and again all earths interconnected. The first connector had a single BNC-connector in the other end and is illustrated in **Fig. 4.4C**, which allowed for simultaneous driving of all the transducers with a single amplifier. The second connector can be used to drive individual transducers.

It should be noted that the transducer cable length shown in **Fig. 4.4C** is not representative, as these were made to have the same length, to ensure similarity. The picture in **Figure 4.3** illustrates this as well.

3.3 Material characterisation

As mentioned in **Section 2.5.3**, the backing of the transducer plays an important role for the resulting sound field. Therefore, in order to find the right type of backing, multiple different samples were made to evaluate their acoustic characteristics. The samples were prepared using EpoFix epoxy (Struers A/S, Ballerup, Denmark) as the base constituent, with two types of particle dopings; one with

high and one with low density. The low density particles were K1 glass balloon (3M, St.Paul, MN), which are 65-μm hollow glass spheres with a density of $\rho = 125\,\mathrm{kgm}^{-3}$ [58]. The high density particles were 99.95%-pure 5-μm tungsten particles (Metallhuset Bergse A/S, Lierskogen, Norway), where the density of tungsten is $\rho = 19250\,\mathrm{kgm}^{-3}$ [59]. Although, the treatment devices produced in this thesis were required to have a light backing, increasing the power output, backing samples with a high acoustic impedance were also produced and analysed. This was in case future devices require reduced ringing and a greater bandwidth.

Four samples were made with tungsten dopant at a tungsten-epoxy weight ratio of 1:3, 1:3.5, 1:4 and 1:4.4. Three samples were made with glass balloon doping, at a glass balloon-epoxy weight ratio of 8:1, 10:1, and 11:1. In addition a sample without any dopant was made as a control.

After mixing, each mixture was degassed in a vacuum chamber to remove air pockets. The samples were cycled between 0.5mBar and atmospheric pressure 20 times, until no air bubbles could be seen on top of the sample.

The mixtures were then poured into $\varnothing 55\,\mathrm{mm}$, 6-mm high, circular plastic petri dishes. Thereafter, they were placed the vacuum chamber, and exposed to a partial vacuum of 0.5mBar another 20 times, to ensure no new air pockets were made after pouring the samples from the mixing cup to the petri dishes.

The samples were then left to cure for 24 hours, thereafter the petri dish was broken away from the sample. The surface that was not in contact with the mould was left with a elevated ring around the edges. This was removed using fine sandpaper (P180, 3M, St. Paul, MN).

The thickness, d_s, of the finished samples were measured using a micrometer screw gauge (Mitutoyo, Kanagawa, Japan) with 20 measurements at separate locations around the disk. The diameter, $2r$, was measured using a digital caliper (Mitutoyo, Kanagawa, Japan), also at multiple separate locations. Thus, after weighing the samples, the density:

$$\rho = \frac{m}{\pi r^2 d_s},$$

could be calculated, where m is the mass measured, r is the radius, and d_s is the thickness of the samples.

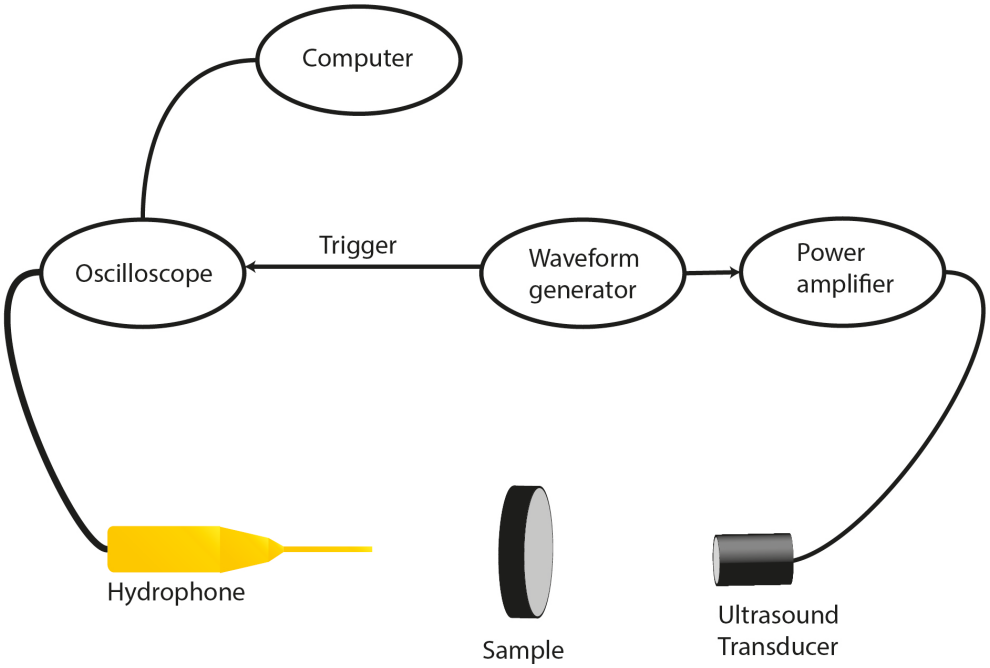

Figure 3.3: Connection schematic depicting the experimental setup and equipment connections for the material characterisation.

The speed of sound was measured using the transit time method [49]. The experimental setup used can be seen in **Figure 3.3**. Primarily reference measurements were performed, placing the hydrophone co-axially at an arbitrary distance from the transducer. The transducer was a 1-MHz single element transducer, and it was driven by a waveform generator (AFG3002, Tektronix Inc., Beaverton, OR) connected to a RF power amplifier (A150, Precision Acoustics, Dorset, United Kingdom) with a 5-cycle sinusoidal burst-wave at 1 MHz. Five cycles were used, as this was sufficient to create a transient state wave. This was determined by doing a fast fourier transform (FFT), of the signal received by the hydrophone, and increasing the number of cycles until no changes were seen in the frequency spectre created by the FFT. The transit time, t_1, was measured by using the cursor function on the oscilloscope (TDS3012, Tektronix Inc., Beaverton, OR), measuring the time since the trigger was sent out from the waveform generator, to the signal received by the hydrophone, connected to the oscilloscope. This measurement was performed 8 times in order to get an estimation of the random uncertainty.

Without changing the distance between the transducer and the hydrophone, a sample was inserted between the hydrophone and the transducer, as demonstrated in **Figure 3.3**. The total transit time while the sample was inserted, t_2, was then measured analogous to the measurement performed without the sample inserted. This was performed for all 8 samples. The speed of sound could then be calculated using **Equation 2.23**, in combination with **Equation 2.24**.

3.4 Calibration and characterisation

The sound field calibration of the transducers was performed in a custom made $100 \times 55 \times 40\,\text{cm}$ (220 L) perspex calibration tank as seen in **Figure 3.6**. This tank was designed to perform several types of ultrasonic characterisations, but primarily field scans; a spatial mapping of the pressure distribution of the ultrasound field. The waveform generator, oscilloscope and the 3D linear stage system (Zaber Technologies Inc., Vancouver, BC) were all controlled by a computer, via a custom LabVIEW® (National Instruments Corporation, Austin, TX) program.

Prior to all measurements, it was ensured that the water in the scanning tank would meet the requirements of the IEC standard on measuring medical ultrasonic fields [47]. For this reason, distilled water was used. Furthermore, the water was also degassed, using the pump seen in the bottom right in **Figure 3.6**. This technique works by turning on the pump, and restricting the inlet valve supplying the water to the pump, which creates a partial vacuum, causing gas to conglomerate into larger bubbles, which when fed back into the tank, will rise to the top of the water and escape. Using this technique a sufficiently low gas content in the water can be achieved [60]. The water temperature was also checked, to ensure no major deviation from 20 °C, as this was the temperature of the hydrophone calibration.

Whenever the hydrophone was used it was placed in water to soak before usage, as the hydrophone requires up to 1 hour of soaking time before the output stabilises. A calibrated $\varnothing 200\,\mu$m PVDF needle hydrophone was used, (Precision Acoustics Ltd, Dorset, United Kingdom), calibrated in steps of 1 MHz from 1 to 30 MHz by the manufacturer. The hydrophone was mounted on to the 3D linear stage system via an aluminium rod and a custom made 3D-printed hydrophone

mount (**Fig. 3.4**). This mount was constructed to minimize reflections sent towards the sensing element of the hydrophone.

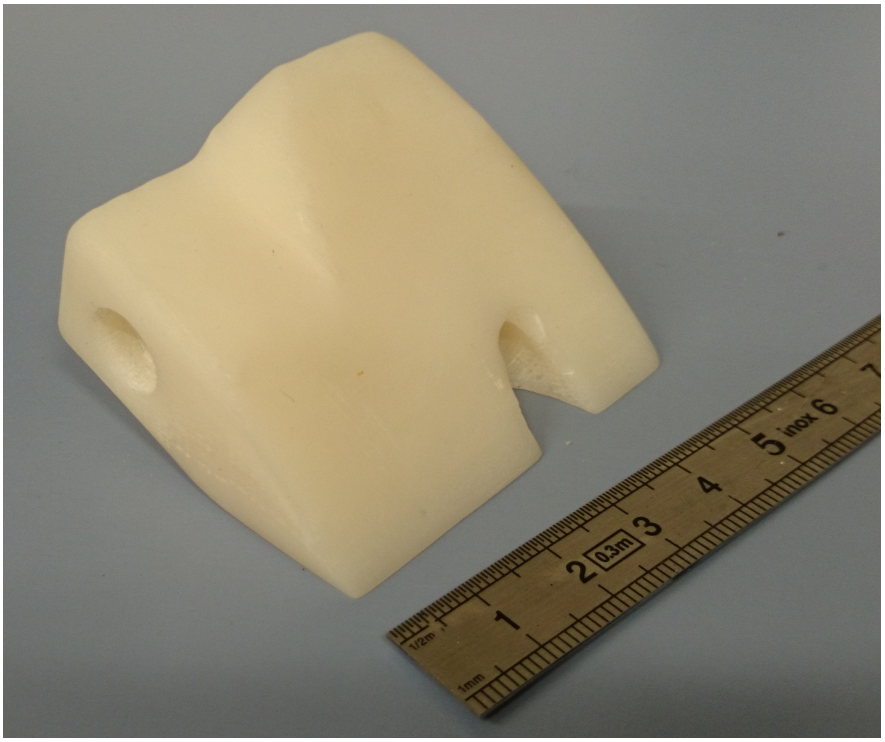

Figure 3.4: Photograph of the 3D-printed hydrophone mounting device, designed to reduce reflections towards the hydrophone sensing element.

In order to simplify the presentation of the measurement techniques, a coordinate system was used. The longest dimension of the tank, which is also the direction of propagation, will hereby be denoted the z-axis, upwards, the y-axis, and the perpendicular to these, the x-axis.

The linear stage system consisted of 3 motorized stages and one support stage, to increase stability. In the x- and z-direction a 300 mm A-LSQ-300B (Zaber) was used, with an extra 300 mm LSQ-300G (Zaber) support stage in the z-direction. In the y-direction a 300 mm T-LSR-300B (Zaber) was used. They were all controlled via a T-JOY3 (Zaber), which was connected to a computer, allowing computer control. All of the motorized stages were closed loop, which means they can always report their absolute position, and will perform auto-correction of their position after moving. They had an accuracy of 30 μm, with a

repeatability $< 2.5\,\mu$m and a resolution of $0.4\,\mu$m. While the sensing element of the hydrophone is $\varnothing 200\,\mu$m, it is clear that the potential spatial resolution of a field scan is limited by the size of the sensing elements, as moving the stages at a distance smaller than this will cause aliasing [Reference].

3.4.1 Acoustic frequency characterisation

The first underwater calibration performed was the acoustic frequency characterisation. This was done using a pulse-receive method [61, 62], a method using the transmit and receive capabilities of the transducers to find the frequency with the highest received signal amplitude.

Primarily the bottom plate of the devices was faced against a wall as illustrated in **Figure 3.6**. The waveform generator was connected to the oscilloscope and the transducers in the base plate as seen in **Figure 3.5**. It was set to send out a sinusoidal burst-wave with 5 cycles at $10\,Vpp$ to the transducers and the oscilloscope via a coaxial T-connector. The frequency used for the initial set-up was the frequency of the lowest reflection coefficient ($\sim 1\,$MHz). The oscilloscope window was then panned so only the reflected wave was recorded, thus the higher drive voltage pulse was not measured. In addition, the voltage divider setting on the oscilloscope was tuned in such that the signal had an as high resolution as possible without clipping.

Thereafter, the device was rotated and pitched manually, and locked in place at the orientation which produced the largest signal on the oscilloscope.

Following the initial setup, a computer controlled linear frequency sweep was performed. The frequency sweep was performed from 400 kHz to 5 MHz with 500 samples, yielding a step size of 9.2 kHz. For each sample the computer would set the waveform generator to a specific frequency, and subsequently read the maximum peak-to-peak voltage from the oscilloscope. After the scan was performed, all the voltages were divided by the highest recorded voltage, normalising the amplitude values.

From this data, several parameters were extracted and calculated. The center frequency, $-3\,$dB bandwidth, percentage bandwidth and quality factor was calculated using **Equation 2.12-2.15**.

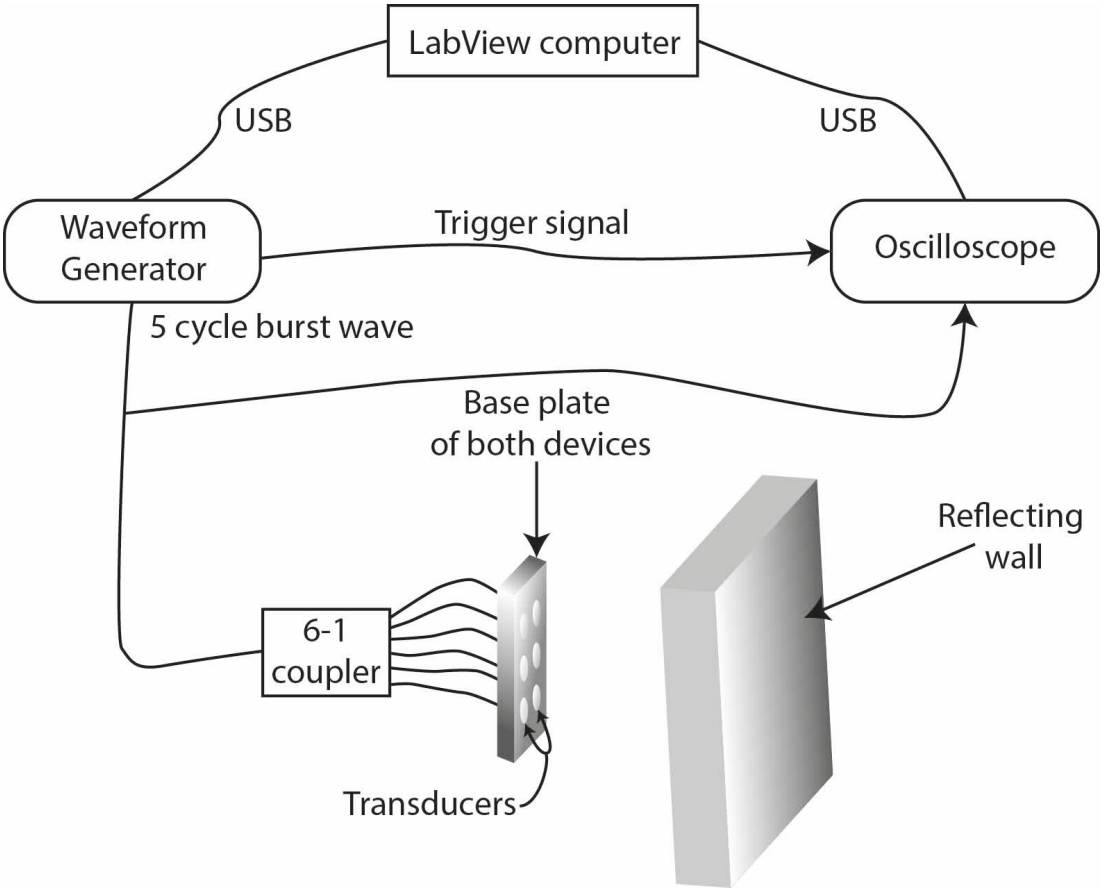

Figure 3.5: Experimental set-up of the acoustic frequency characterization using a pulse-receive method.

The benefits of using such a technique is that it does not rely on the transducers being calibrated prior to measurement, as one only needs the highest relative amplitude the received signals.

3.4.2 Field scan

The initial set up of the field scan, was performed by optically orientating hydrophone parallel and the base plate perpendicular to the z-axis (**Fig. 3.7**). This is an essential step, as the directivity of the hydrophone as well as the transducers can cause an underestimation of the pressure measured if they are not properly aligned.

The field scans were performed using a point sampling method; moving the

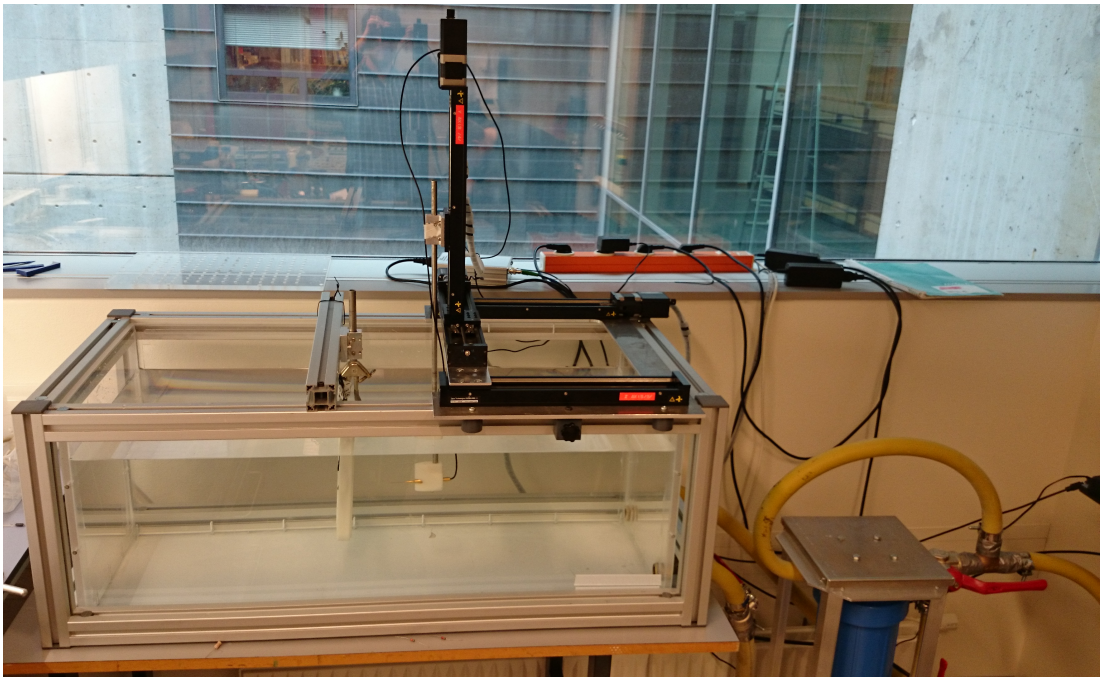

Figure 3.6: Photograph of the custom made ultrasound field characterisation scanning tank. The hydrophone is mounted to the motorized linear stage system, and the bottom plate of device B is held in front of it with a clamp. At the bottom right of the picture is the pump used to filter and degas the water.

hydrophone in the sound field of the transducers, using the 3D linear stage system. The LabVIEW program written to perform the field scan would move the stages, and read 3 parameters from the aquiered signal on the oscilloscope; peak-positive (V_+), peak-negative (V_-) and peak-to-peak (V_{pp}) voltages. Using the hydrophone calibration values, the program would then calculate the acoustic pressure corresponding to the voltages read out.

During the field scan, all elements in the device were driven simultaneously using a five cycle tone burst generated by the waveform generator connected to the RF power amplifier via a $-20\,\mathrm{dB}$ RF attenuator. The frequency used was the center frequency, f_c, found in **Section 3.4.1**. The burst period was set to $1\,\mathrm{ms}$, ensuring that there were no reflections from the previous signal when the next pulse was observed. The attenuator was used to protect the amplifier from voltages surpassing $1\,\mathrm{V_{rms}}$, as the maximum output from the waveform generator is $7\,\mathrm{V_{rms}}$, and the amplifier has a maximum voltage input rating of $1\,\mathrm{V_{rms}}$. Using

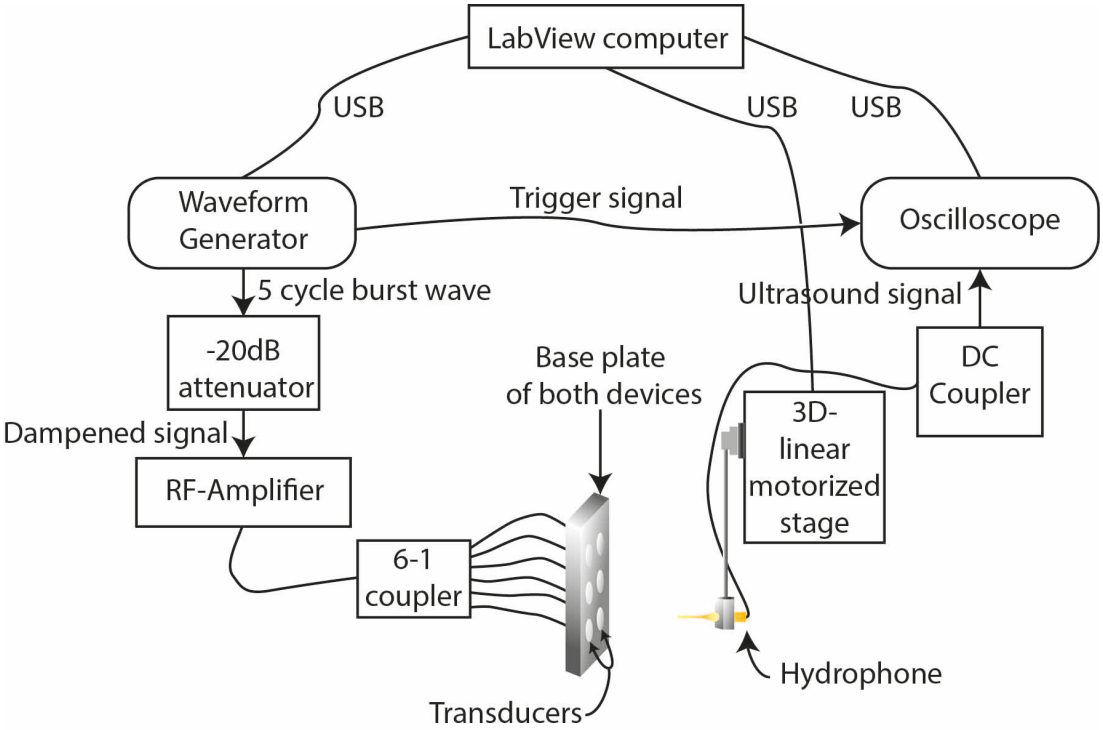

Figure 3.7: Connection schematic depicting the experimental setup and equipment connections for the ultrasound field scan.

the integrated power meter in the amplifier, it was confirmed that it was still possible to achieve maximum power output by the amplifier while using this attenuator.

Similarly to the acoustic frequency characterisation, the oscilloscope voltage divider was set as high as possible, without clipping when the hydrophone was placed approximately in the focus of the transducers. Additionally the time divider was set such that the signal would not go outside the sampling region when the stage was moved in the z direction.

Several 2D field scans were performed for each device. At the distance of the acoustic focus, xy-scans were preformed. This would allow to calculate the full width half maximum (FWHM) area of the focus of each transducer. In addition, xz-scans were performed in order to visualise the distribution of the sound field in the direction of propagation.

3.4.3 Voltage ramp

The experimental setup for the voltage ramp was exactly the same as for the field scan (*cf.* **Fig. 3.7**). The focus of each transducer was found using an localization algorithm, designed to find the location of the highest pressure within a region entered into the program. When the hydrophone was placed in the focus of the transducer, a voltage ramp was performed. This was done by increasing the voltage output from the waveform generator incrementally from 0.2 V to 9 V in 50 steps. As with the field scan, the computer would read the same three parameters from the oscilloscope, converting them to pressures.

This characterisation is highly important for future experiments, as this will correlate input voltages from the waveform generator to pressures.

3.5 Simulations

Whilst performing physical measurements of the acoustic field in these chambers may be technically possible, it requires modifications of the cell culture chambers themselves. As a consequence modifying the acoustic fields. Hence, 4 dimensional finite element simulations were performed to predict the pressure distributions within the closed cell culture chambers. Simulations were performed with PZFlex2015 (Weidlinger Associates Inc., New York, NY).

The setups were reconstructed using an axis-symmetric revolved model consisting of a single transducer (**Fig. 3.8**). The transducers were designed using existing material properties available within the software package. Custom material properties were made for the backing material based on the results from **Section 4.1**. Polyethylene was used to mimic the 3D-print material. The cell culture chamber material of both the PetakaG3^{TM} and the 24-well plate was polyethylene. The thin film materials were Ethylene-vinyl acetate.

The cell culture and microbubble medium was based on properties measured by Hensel *et. al* and Tang *et. al* [33, 63] Two different models were made, one for each device. All dimensions in the simulation duplicated reality. An initial simulation was performed to replicate the free field behavior of the experimental setup. Subsequently, the 24-well plate or PetakaG3^{TM} were placed in their

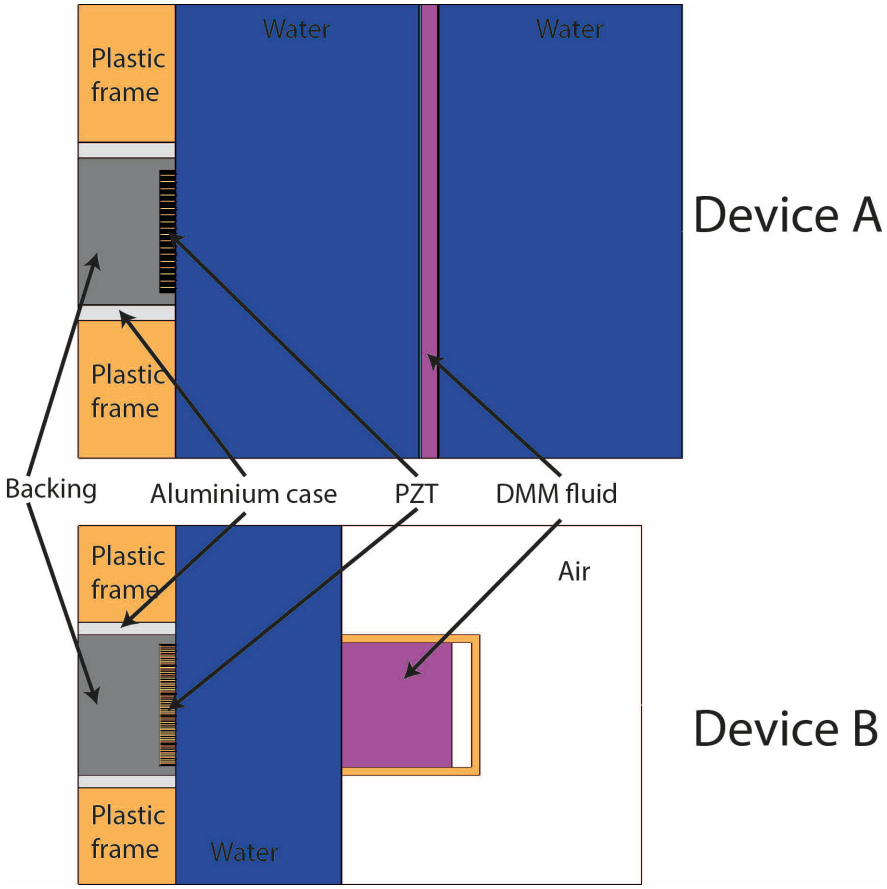

Figure 3.8: Layout of the simulation models. The top drawing is the layout for a single transducer in device A, including an OptiCell^{TM} or PetakaG3^{TM} within the water. The bottom drawing is the layout for a single transducer in device B including a single well of the 24-well plate.

corresponding locations.

The element size used was 50 elements per wavelength. The drive frequency used was 1.019 MHz. Two pulses were evaluated; a 4-cycle and a 34-cycle sinusoidal burst with a pulse repetition period of 100 μs was used. Acoustic pressure field convergence was seen after four pulses, hence both simulations consisted of four pulse repetitions, *i.e.* a total time of 500 μs.

The transient wave from every element in the simulations was captured, and the simulation data was derived from this. From this data pressure maps were reconstructed. Hence we were able to evaluate the effect of placing the cell culture chambers in the acoustic field.

Chapter 4

Results and discussion

4.1 Material Characterisation

In **Figure 4.1** the speed of sound, density, and acoustic impedance is plotted against doping weight ratio. Both graphs start out at 0% weight ratio, which is the control sample made without dopant.

When the epoxy was doped with glass balloons the speed of sound decreased from 2580m s^{-1} for the control sample, to 2260m s^{-1}, for the sample with the highest weigth ratio, at 11%. The density was decreased from 1120 kgm^{-3} to 540 kgm^{-3}, causing a drop in acoustic impedance from 2.89 MRayl to 1.22 MRayl.

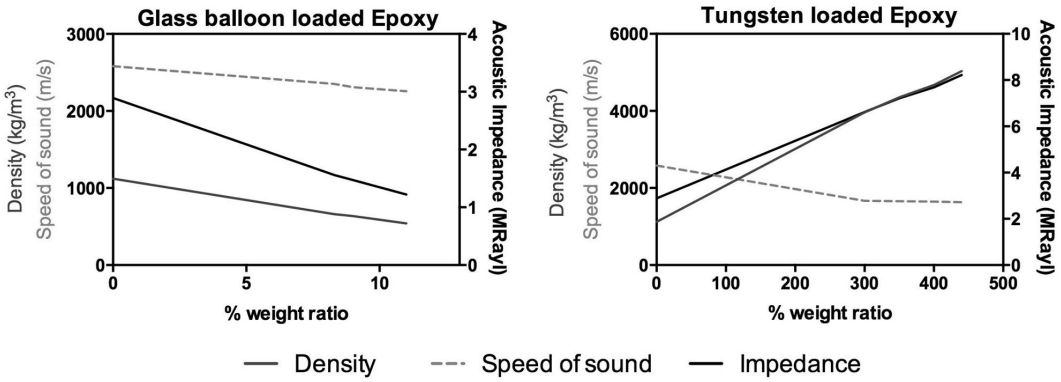

Figure 4.1: Graphs depicting the speed of sound, density and acoustic impedance for all the samples made as a function of weight ratio of dopant.

The epoxy loaded with tungsten particles displayed a larger decrease in the speed of sound compared to the unloaded control sample, decreasing to $1633\,\mathrm{ms}^{-1}$ for the sample with the highest weight ratio of 440%. As expected the density significantly increased in the tungsten loaded samples, up to $5030\,\mathrm{kgm}^{-3}$ for the heaviest sample, yielding a net increase in the acoustic impedance, to 8.22 MRayl.

The results closely matched results obtained for similar mixtures found in literature [43, 64]. Unfortunately the mixture ratios used have to be considered the near maximum usable ratios, whilst maintaining a homogeneous mixture. This was due to the increased viscosity of the finished mixtures at higher weight ratios would not allow degassing of the composite, leaving large gas pockets inside the finished sample.

Using these properties it is possible to modify transducers as needed, making them more broadband by using a tungsten-epoxy composite as a backing layer Conversely they could be made narrowband by using a glass balloon-epoxy composite.

4.2 Electrical impedance measurements and matching

Table 4.1 shows some of the impedances of the transducers in device A. The 6 transducers listed are the impedance values for all the transducers prior to impedance matching. The impedances listed were the values measured at 1.00 MHz, the frequency with the most similar reflection coefficient magnitude, δ. The mean resistance value before impedance matching was $109 \pm 13\,\Omega$, where the error is the standard deviation between the ultrasound transducers. The mean reactance was $-50 \pm 11\,\Omega$. When the impedance matching network was added to each transducers, a new impedance scan was performed. The mean value of the impedance for all the transducers at the lowest δ-value was $65 \pm 12 - (9 \pm 9)i\,\Omega$, at 1.01 MHz. Showing a slight increase in the electrical resonance frequency of the transducers. Furthermore, when all devices were connected in series with the DB-25-connector (*cf.* **Fig. 4.4C**) the impedance value decreased to $44.2 - 6.2i\,\Omega$ at the electrical resonance frequency. A further increase in the electrical resonance

Transducer	Resistance [Ω]	Reactance [Ω]	Frequency [MHz]
1	115.8	-39.3	1.00
2	108.7	-64.6	1.00
3	116.5	-38.6	1.00
4	103.4	-58.6	1.00
5	124.9	-41.1	1.00
6	86.4	-55.6	1.00
Mean before matching	109 ± 13	-50 ± 11	1.00
Impedance matched	65 ± 12	-9 ± 9	1.01
Combined	44.2	-6.2	1.10

Table 4.1: The impedances of Device A measured at the frequency of the lowest electrical reflection coefficient magnitude. The individual transducers listed here are prior to impedance matching, with the mean value of all of them below. Below that is the mean of all the devices with the impedance matching network connected. Combined is an impedance measurement for all the devices connected in series.

frequency to 1.10 MHz was observed.

Table 4.2 shows the analogous measurements of device B. Prior to impedance matching the mean impedance of the transducers was $76 \pm 24 - (50 \pm 21)i\,\Omega$ at a frequency of 0.96 MHz. The dissimilarity in electrical impedance between the transducers in device B prior to matching was significantly larger than that of the transducers in device A. The mean value for the impedance matched transducers was $28 \pm -(10 \pm 6)\,\Omega$, however no shift in the electrical resonance frequency was observed. Nevertheless, when all transducers were connected in series a larger frequency shift was observed, increasing to 1.14 MHz. In addition, when they were connected in series the impedance was increased to $58.7 + 2.7i\,\Omega$. Both devices showed that when connected in series they were quite close to the perfect electrical impedance match of $50 + 0i\,\Omega$.

The electrical reflection coefficients as a function of frequency, calculated from the impedance values with **eq. 2.19** is shown in **Figure 4.2A** and **B** for device A and B, respectively. The traces before and after impedance matching are the mean electrical reflection coefficient of all transducers, while all elements joined is the result of a single impedance scan of all elements connected in series. As was expected, the reflection coefficient dropped significantly after impedance matching for both devices. Although not present in the transducers individually,

Transducer	Resistance [Ω]	Reactance [Ω]	Frequency [MHz]
1	50.4	-77.9	0.96
2	98.5	-33.2	0.96
3	88.8	-28.3	0.96
4	77.5	-52.1	0.96
5	97.6	-37.7	0.96
6	43.3	-72.2	0.96
Mean before matching	76 ± 24	-50 ± 21	0.96
Impedance matched	28 ± 7	-10 ± 6	0.96
Combined	58.7	2.7	1.14

Table 4.2: The impedances of Device B measured at the frequency of the lowest electrical reflection coefficient magnitude. The individual transducers listed here are prior to impedance matching, with the mean value of all of them below. Below that is the mean of all the devices with the impedance matching network connected. Combined is an impedance measurement for all the devices connected in series.

the reflection coefficient at the 3rd harmonic was significantly reduced when all the transducers were connected in series. This occurred for both devices. The transducers in device A had a mean lowest reflection coefficient magnitude of $\delta = 0.45$ prior to impedance matching and $\delta = 0.19$ after impedance matching, with a further drop down to $\delta = 0.09$ after all transducers were interconnected. In device B a similar trend was observed with $\delta = 0.46$ prior to impedance matching, $\delta = 0.16$ after impedance matching and $\delta = 0.08$ when all transducers were interconnected. Furthermore, comparing the two plots, the identically constructed transducers in device B are seen to have a large drop in the electrical reflection coefficient magnitude below the resonance frequency.

The discrepancy in the reflection coefficient of the transducers in device B was also predicted by the impedance values. This might be due to the inexperience of the construction process when building the first batch of transducers for device B. Although the electrical reflection coefficient magnitude will not necessarily tell how the devices will perform acoustically, it gives a very informative view of the electrical behavior of the transducer circuit. Furthermore, it allows to compact a lot of data in a simple graph.

The impedance magnitude for the transducers in device A prior to impedance matching was $I_{\text{mag,A}} = 120 \pm 17\,\Omega$ at 1.00 MHz. While the transducers in device

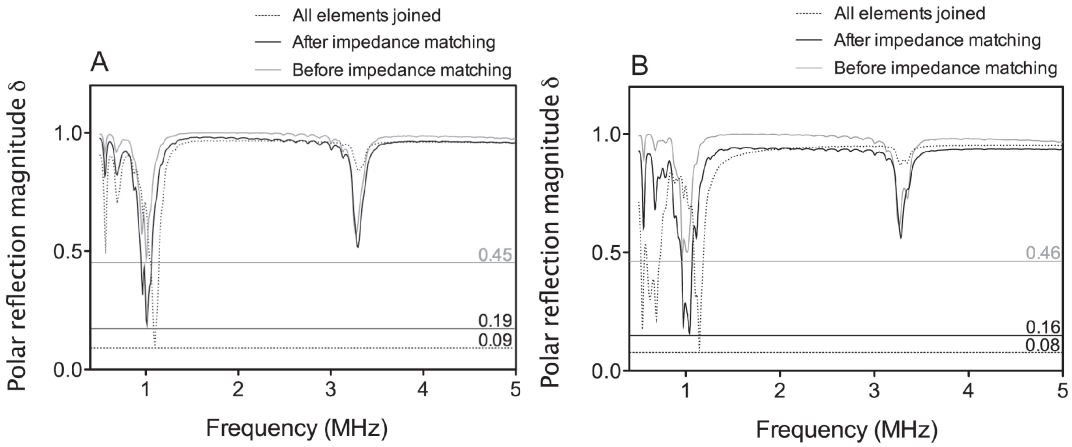

Figure 4.2: Electrical reflection coefficient as a function of frequency for both devices, with and without impedance matching. Mean polar reflection magnitude (δ) as a function of frequency for the device A (A) and device B (B) A minimum reflection can be seen at the centre frequencies and reduced reflections at the equivalent third harmonics. After impedance matching, the reflection coefficient is significantly reduced at the centre frequency but not at the third harmonic. Connecting all elements in a device together reduces the reflection coefficient further more.

B had an impedance magnitude of $I_{\mathrm{mag,B}} = 91 \pm 32\,\Omega$ at 0.96 MHz.

The TLT designs were taken from [57]. A design that would match $I_{\mathrm{mag,B}}$ to $50\,\Omega$ was W2FMI-2.25:1-HU50 [57]. This is a ferrite toroidal core transformer with 6 trifiliar turns through the center of the core. However, during the construction of the transformer, it was discovered that an alteration of this design would produce an even better match to $50\,\Omega$, by adding a seventh trifiliar turn. The schematics for this alternated design can be seen in **Figure 4.4A**

The design chosen to ameliorate the electrical performance of the transducers in device A was W2FMI-2.25:1-HU112. This design is very similar to the one used for the transducer in device B and is reproduced in **Figure 4.4B**.

In order to simplify construction for inexperienced users, a color-coded model was also made, also visible in **Figure 4.4A-B**. The final assembly of the base plate of device B with all transducers inserted, connected to TLTs and DB-25-connectors can be seen in **Figure 4.3**.

Although the transducers were made with different TLTs there did not seem to be any significant differences introduced because of the differences in the TLTs.

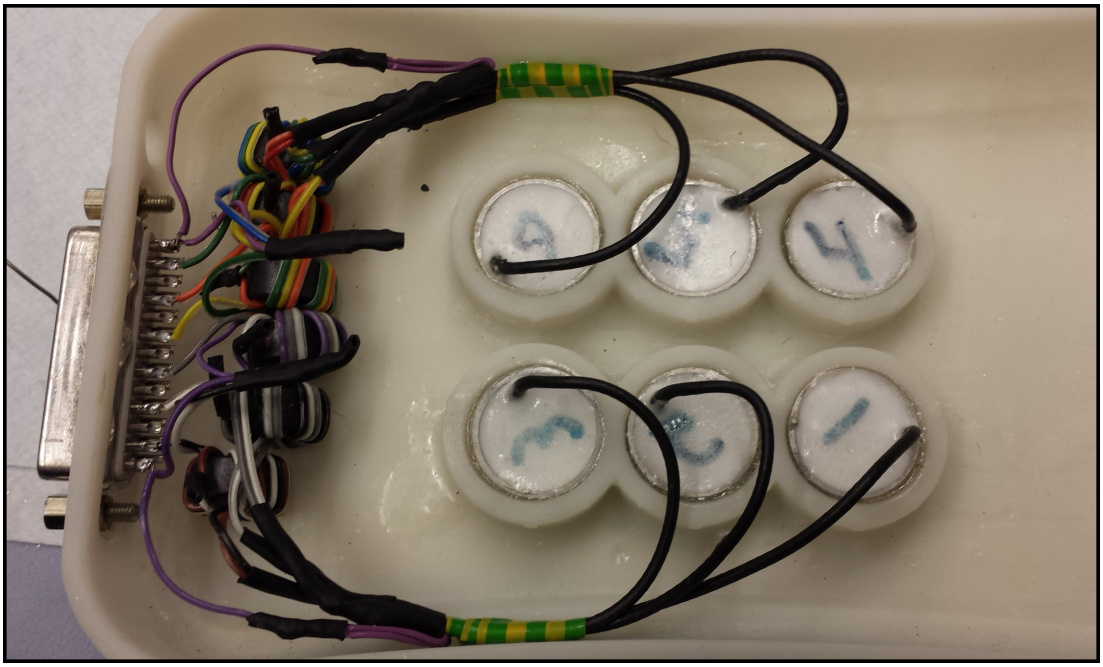

Figure 4.3: Underside of Device B, the numbered white cylinders are the backsides of the transducers, with the coaxial cable going out from them. All transducers are connected to their own TLT, in turn connected to the DB-25 female connector.

TLTs were very straight-forward to manufacture, an important feature of the sonicators. The electrical impedances scans revealed that they were very effective for improving the electrical performance of the devices.

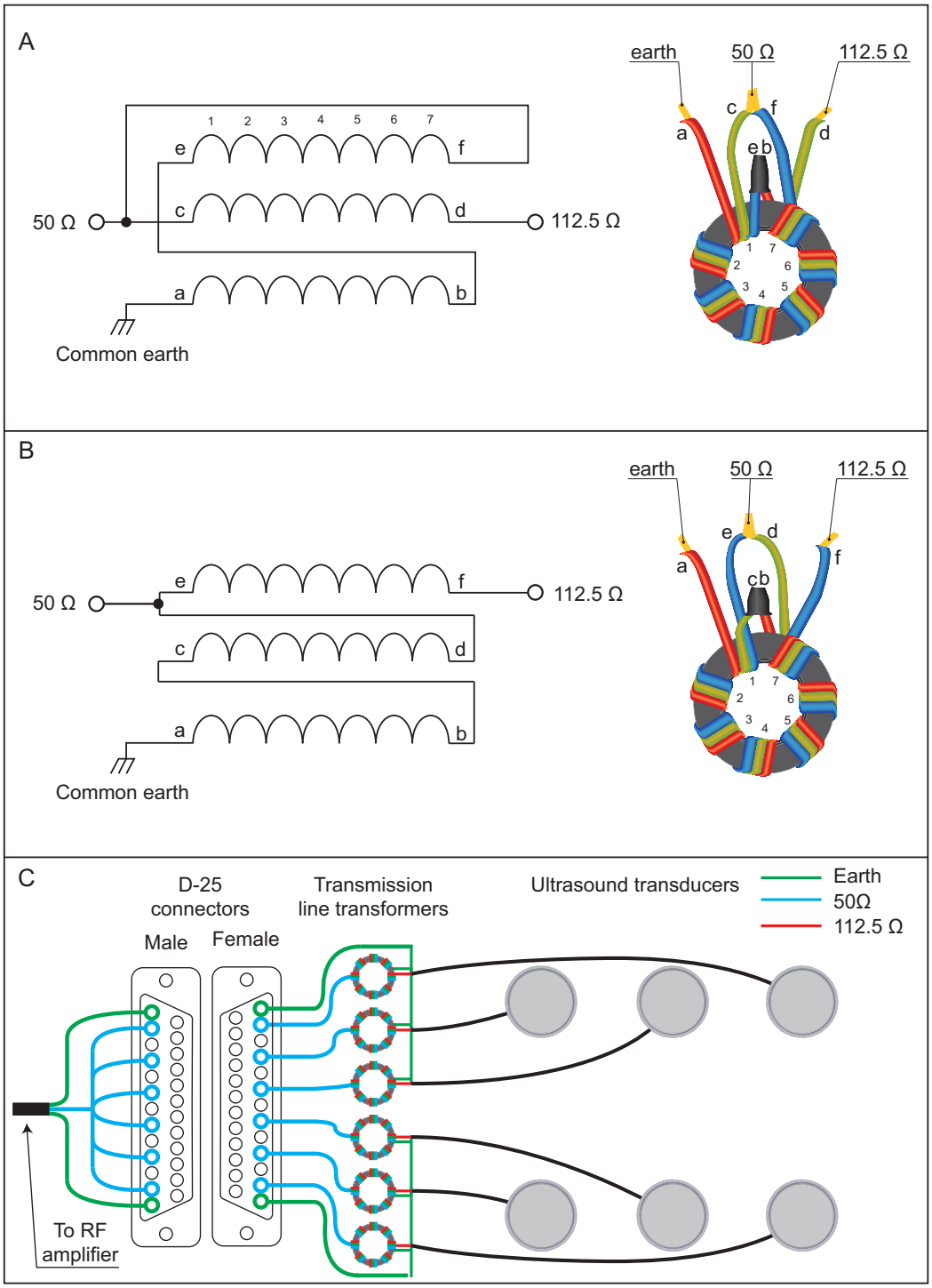

Figure 4.4: Electrical impedance matching and connection diagrams. Transmission line transformers used to match 112.5− transducers to 50 Ω (A and B). Both variation result in the same impedance ratio and can be used interchangeably. Wiring schematic from transducers to amplifier (C) showing the independent connection of each transducer in the case. All transducers can be driven simultaneously via an inter-connected male connector.Schematics of the transmission line transformer for the transducers of device A.

4.3 Acoustic frequency response

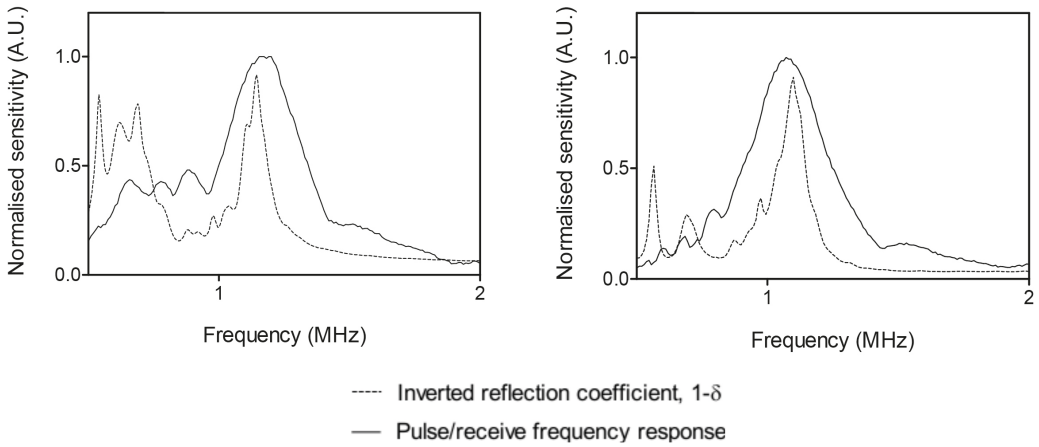

Figure 4.5: Normalized frequency response and inverted electrical reflection coefficient $1-\delta$ plotted against frequency for the devices. A direct correlation can be seen between the electrical refleciton coefficient magnitude and the acoustic frequency response data.

The acoustic frequency response measured by the pulse-echo method for both devices is shown in **Fig. 4.6**. The pulse-echo method of finding the resonance frequency of the transducers correlated well to the electrical reflection coefficient magnitude for both the devices. The third harmonic, located around 3 MHz was not observed in these scans either, as predicted by the electrical impedance measurements. As with the reflection coefficient magnitude, device B had a frequency of highest response at a frequency higher than device A. Device A had a frequency of highest response of 1.08 MHz, while device B had its highest response at 1.17 MHz. Furthermore, device B had a significantly higher response between 0.6 and 0.8 MHz, which directly correlates to the reflection coefficient. This correlation also visible in **Figure 4.5**, where the inverted reflection coefficient magnitude, $1-\delta$, and the acoustic frequency response is plotted against frequency. The peaks of the frequency sensitivities were smoother than those of the reflection coefficient, due to the mechanical response of the transducers. Furthermore, the peak sensitivity frequency was lower than that of the electrical resonance for device A, while the opposite effect was observed for device B. The frequency of the highest acoustic frequency response for device A was 0.03 MHz lower than

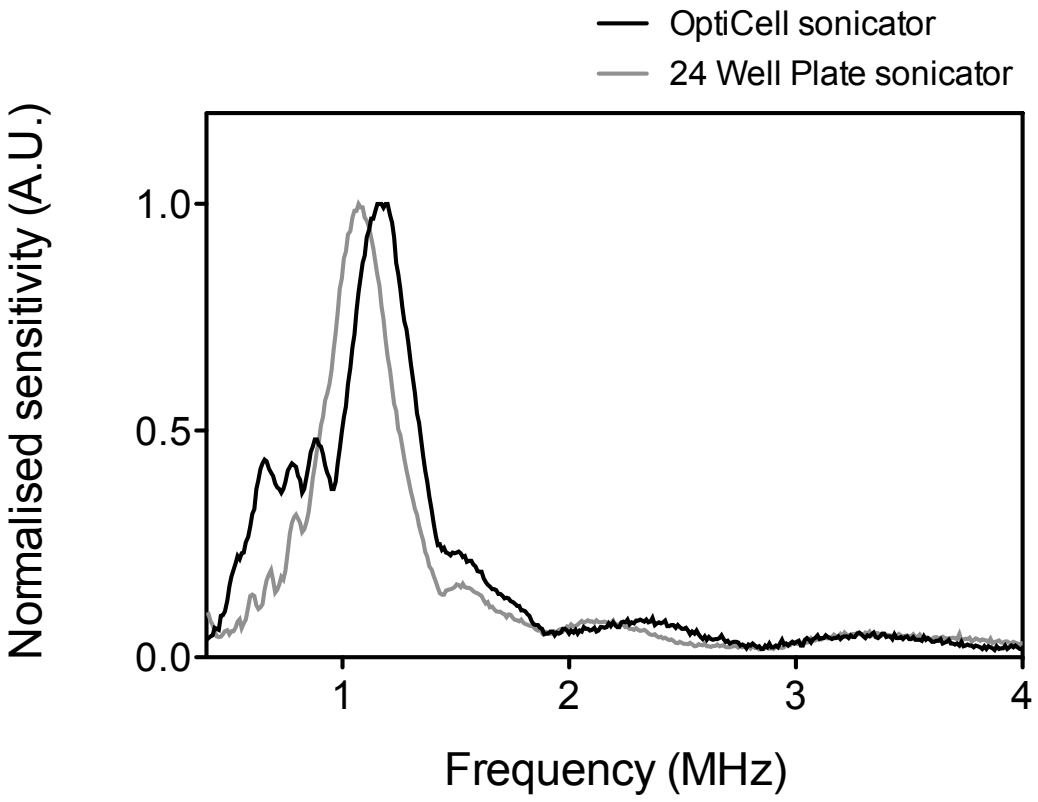

Figure 4.6: Frequency sensitivity of sonicators. Peak sensitivity canbe seen at 1.08 and 1.17 MHz for the 24-well plate and OptiCell^{TM} sonicator, respectively. Increased sensitivity is evident between 0.6 and 0.8 MHz in the OptiCell^{TM} sonicator. This directly correlates to the reflection coefficient magnitude shown in **Figure 4.2B**.

the electrical resonance frequency. Whilst for device B it was 0.03 MHz higher.

The frequency constants for both devices calculated using a -3 dB cutoff from the acoustic frequency response can be seen in **Table 4.3**. All frequency constants for device A were consistently lower than those calculated for device B. However, the bandwidth measured was identical, which left the precentage bandwidth lower for the device with the higher frequency constants.

Using this method to determine the frequency for the highest acoustic power output might not be optimal, as the frequency of highest output, and of highest receive sensitivity are different in the same piezoelectric elements [] . However, as these two frequencies are quite close, this method provides a very good es-

	Device A	Device B
Peak sensitivity [MHz]	1.07	1.15
f_{l} [MHz]	0.90	1.00
f_{c} [MHz]	1.08	1.17
f_{u} [MHz]	1.25	1.34
BW [MHz]	0.17	0.17
Q_{m}	6.32	6.86
$\%BW$ [MHz]	15.82	14.57

Table 4.3: Frequency response of sonicators using a -3 dB cut-off. A small centre frequency shift of 90 kHz between devices is evident yet both devices have an identical bandwidth of 170 kHz and a similar mechanical quality factor.

timation of the frequency of highest acoustic output power. There are a few effects that might skew the results, that were not considered in the results, as they were assumed negligible. One that might cause an underestimation of the lower frequencies, is the fact that the ultrasound beam diverges more at lower frequencies, forming a focus closer to the transducer surface. The second effect is the frequency dependent attenuation of sound in water, where the attenuation increases with increasing frequencies, which causes an underestimation of the output of the higher frequencies.

4.4 Field scan

Figure 4.7 show the result of the free field scans for both devices. The top two scans depicted are the xy- and xz-scans for device B, while the bottom scan is the xy-scan for device A. The color mapping displays the normalised spatial pressure distribution. The bright red areas are the areas of the highest pressure, whilst white means no acoustic pressure recorded. In the xy-scans, the individual transducers can be separated, as the red fields are the foci for each of the transducers. An interference pattern is observed in the xy-scan of device B, which is also verified in the xz-scan. This was not observed in the xy-scan of device A, as the spacing between the transducers was significantly larger in this device. Each of the devices were able to create six separate foci, as desired.

Based on the data from the field scans, the mean size of the focal spots was calculated for each device. An unpaired t-test was performed to test if the beam sizes were significantly different for each device. A p-value of $p = 0.0013$ indicated that the beam sizes were significantly different. The mean focal area of the transducers was smaller for Device B at $106 \pm 11\,\mathrm{mm}^2$ compared to $146 \pm 21\,\mathrm{mm}^2$ for Device A (*cf.* **Fig. 4.8C**).

The difference between x and y pressure profiles (*cf.* **Fig. 4.8A-B**) might be due to mis-alignment during the field scans and interference in the sound field between the transducers.

As the devices are made for different uses, and are constructed differently, this will have different consequences for the two of them. The first thing to consider is the influence the wall on the ultrasound field of the devices when they have been assembled. **Figure 4.7** gives a very quick answer to this, as it is evident that there is minimal ultrasound propagation at the sides of the main lobe, thus a potential reflection back from the wall to the samples to be sonicated will not cause a significant difference in the pressure at the location of the sample.

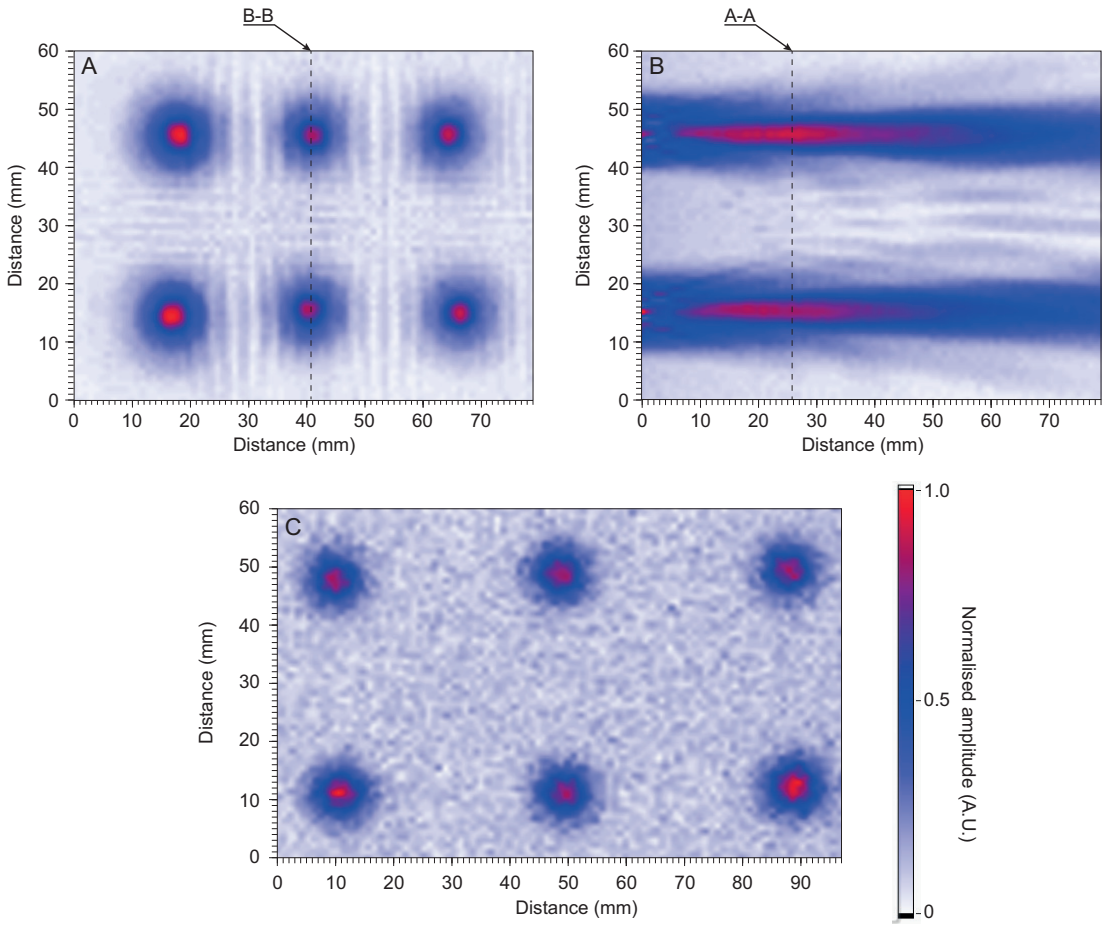

Figure 4.7: Field scans of plate sonicators. Scans A and B are the xy and xz scans of device A sonicator. Line B-B indicates the location of scan B, wheras line A-A indicates the location of scan A. Scan C is the is the xy scan of device A. All scans are at the same scale. Minor side lobes are evident in device B due to the close proximity of the transducers. This was not seen in device A.

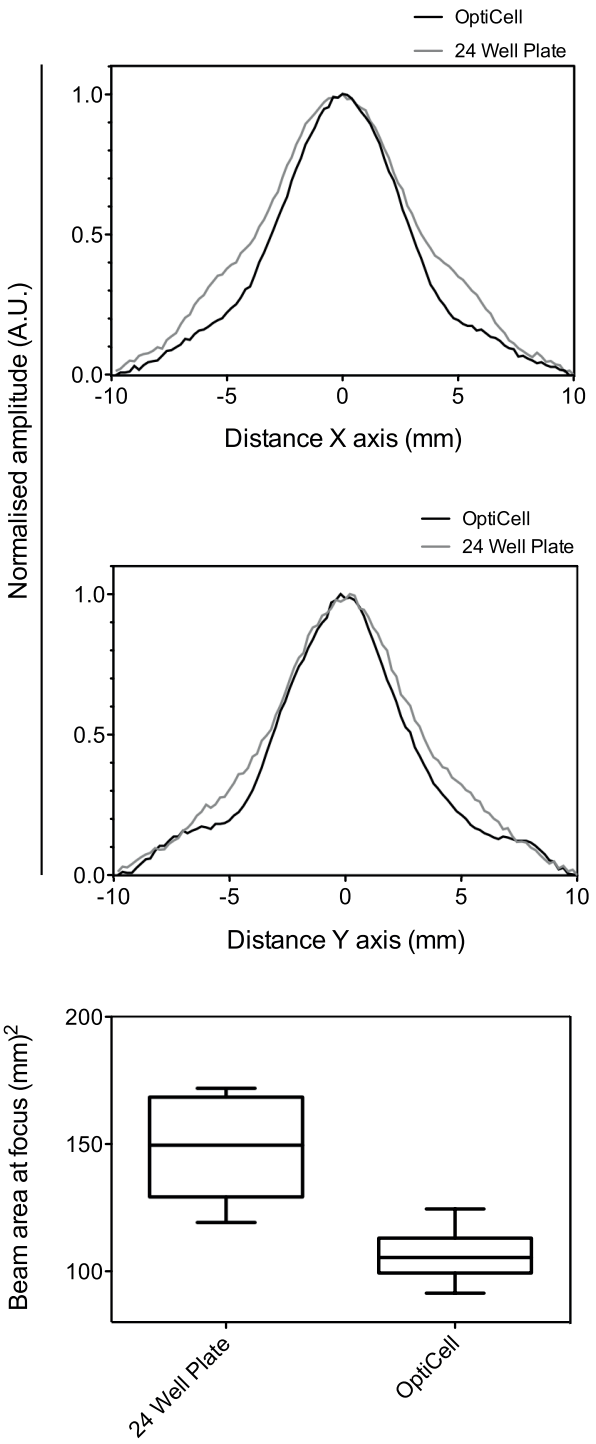

Figure 4.8: Beam profile scans at acoustic focus for both devices and whisker plot of the focal area for the two devices using a -3-dB cutoff. A statistically significantly smaller beam area evident in the device B, due to the close proximity of transducers (cf. **Fig. 4.7**).

4.5 Voltage ramp

Figure 4.9 depcits the performance of these devices in free field conditions. Panel A shows the peak-peak pressure as a function of voltage on the waveform generator. For each device, each transducer was measured separately in the focus of the respective transducer. The error bars indicate the standard deviation between the transducers. The response was approximately linear until it started to taper off at $\sim 8.2\,\mathrm{V_{pp}}$. As this was well within the capabilities of the amplifier, this suggested that the output from the transducers were reaching saturation at this point. The pressures measured were very similar between the devices, with mean values and error bars practically overlapping.

Panel B shows the effect of the electrical impedance matching on a single transducer, by comparing the pressure output of two identical transducers with and without impedance matching. The grey line is a transducer without impedance matching, while black is the same transducer with impedance matching. It is clearly evident that the presure output was significantly larger. At an input voltage of $8\,\mathrm{V_{pp}}$ the impedance matching increased the normalised pressure amplitude from 0.3, to 0.9. Demonstrating an improvement factor of 3. This correlated to the decrease in electrical reflection coefficient.

Panel C shows the mean nonlinearity ratio of the ultrasound waves (**eq. 2.10**) for all the transducers in each device. The nonlinearity ratio very similar for both devices, and was increasing according to the theory of non-linear propagation. When doing bubble experiments this is an undesired effect, hence it is essential to avoid large values of NLR.

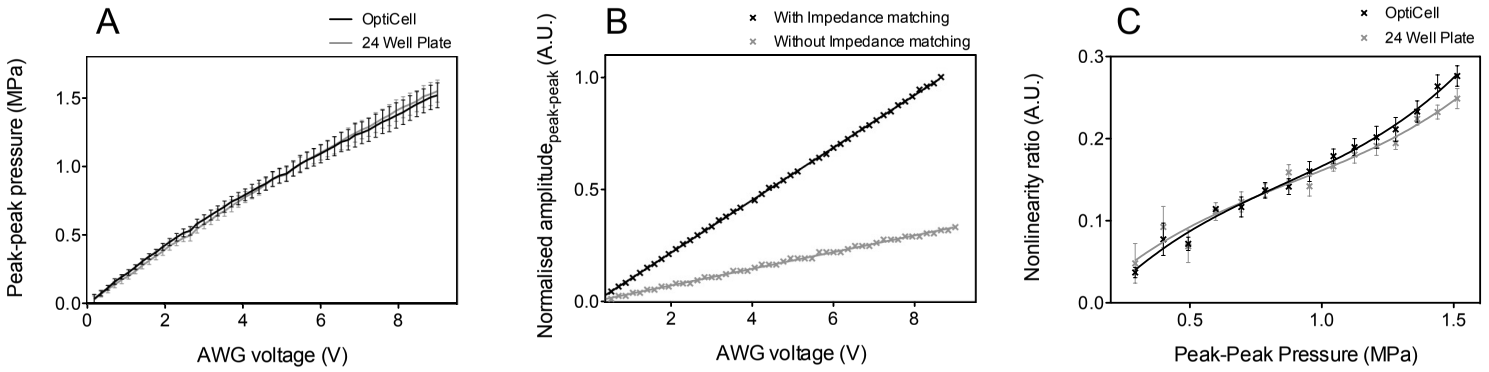

Figure 4.9: Acoustic output from sonicators. Panel A: Mean peak-to-peak acoustic pressure as a function of arbitrary waveform generator (AWG) voltage. The acoustic pressure output is not linear in relation to the voltage input. Panel B: Normalised mean peak-to-peak acoustic pressure as a function of AWG voltage with and without impedance matching. Electrical impedance matching effectively tripled the acoustic output. Panel C: Mean non-linearity ratio a function of mean peak-to-peak acoustic pressure. As acoustic pressure increases, so does the nonlinearity explaining the nonlinear relationship between input voltage and output pressure. Error bars indicate standard deviations.

4.6 3D-printing

Each part required about 8 hours printing time, before post processing and curing. After curing the printing supports were removed with pliers, and remaining irregularities were filed and sanded to even the surface. The first device that was built was device B, and the holes for the transducers were printed slightly too large, which introduced an alignment issue with placing the transducers into the base plate. This was corrected for device A, where the holes were printed slightly smaller which resulted in a tight fit.

Some of the challenges using a 3D-printer was the quality of the finished print, as depending on the orientation during the print, some surfaces were rougher than others. The bottom of the devices, into which the transducers were placed was left with a rough surface caused by the additive layer printing process. This proposed a problem when the transducers were to be inserted, as the epoxy would seep out through the hole as the seal between the UV-tape and the plate was not completely sealed. This problem could have been avoided if this surface was sanded prior to bonding the transducers.

4.7 Transducers construction

The transducers construction was the most challenging part of the building of the devices. As previously stated, for each device all transducers were made simultaneously, but the devices were made at different times. Hence, the transducers for device B was made first, and the only problem experienced during the construction happened to these. The problem was with the backing material, made by a mixture of epoxy and glass bubbles. From the material characterisation of the different samples, the mixture giving the backing with the lowest acoustic impedance was determined. However, this mixture was too viscous, and was forced into place with a toothpick. After curing it was revealed that it was not possible to degas this mixture properly, and several cavities were left around the PZT. In addition, as a result of the forcing of the paste into place, the surfaces of the transducers was not completely flat.

Hence, the transducers for device A were made with a backing that had a

slightly higher acoustic impedance, as this made the construction process significantly easier.

4.8 Simulations

From the simulations, plots analogous to the xz-field scans were plotted (**Fig. 4.10**). Two driving scenarios were modeled; a 4-cycle, and a 34-cycle sinusoidal burst. The top two panels were a model of the transducers radiating in free-field conditions. A noticeable difference in the pressure distribution in the free field was observed for the two different sinusoidal bursts. This indicates that the acoustic field scans performed ought to have been done for multiple different cycles. Furthermore, a more distinct interference pattern was observed when driving with a 34-cycle burst.

The plots for the model simulating the 24-well plate (*i.e.* device A), are the two middle ones. For a 4-cycle burst a significant increase in pressure at the cell culture medium/air-interface was observed. When increasing to a 34-cycle burst, a interference pattern was observed throughout the entire chamber, with a radical pressure increase in center of the cell culture chamber. This was due to complete reflection at the cell culture medium/air-interface.

The PetakaG3$^{\text{TM}}$ design was chosen as it allows transmission through the entire device. However, it was seen that for the 4-cycle case that it would create a slight interference pattern between the first wall and towards the transducer, as well as in inside the cell culture chamber. For the 34-cycle case a more prominent interference pattern was observed.

In order to get a deeper understanding of the acoustic behavior inside the cell culture chambers several axial pressure distributions were also generated from the simulations. These distribution shows the distance from the transducer on the x-axis, and peak-peak pressure on the y-axis (**Fig. 4.11**). Each plot displays two cases; the black line represents the pressure inside the cell culture chambers, while the grey line is superimposed from the free field scan. The dotted vertical lines indicate the location of the acoustic interfaces in the devices.

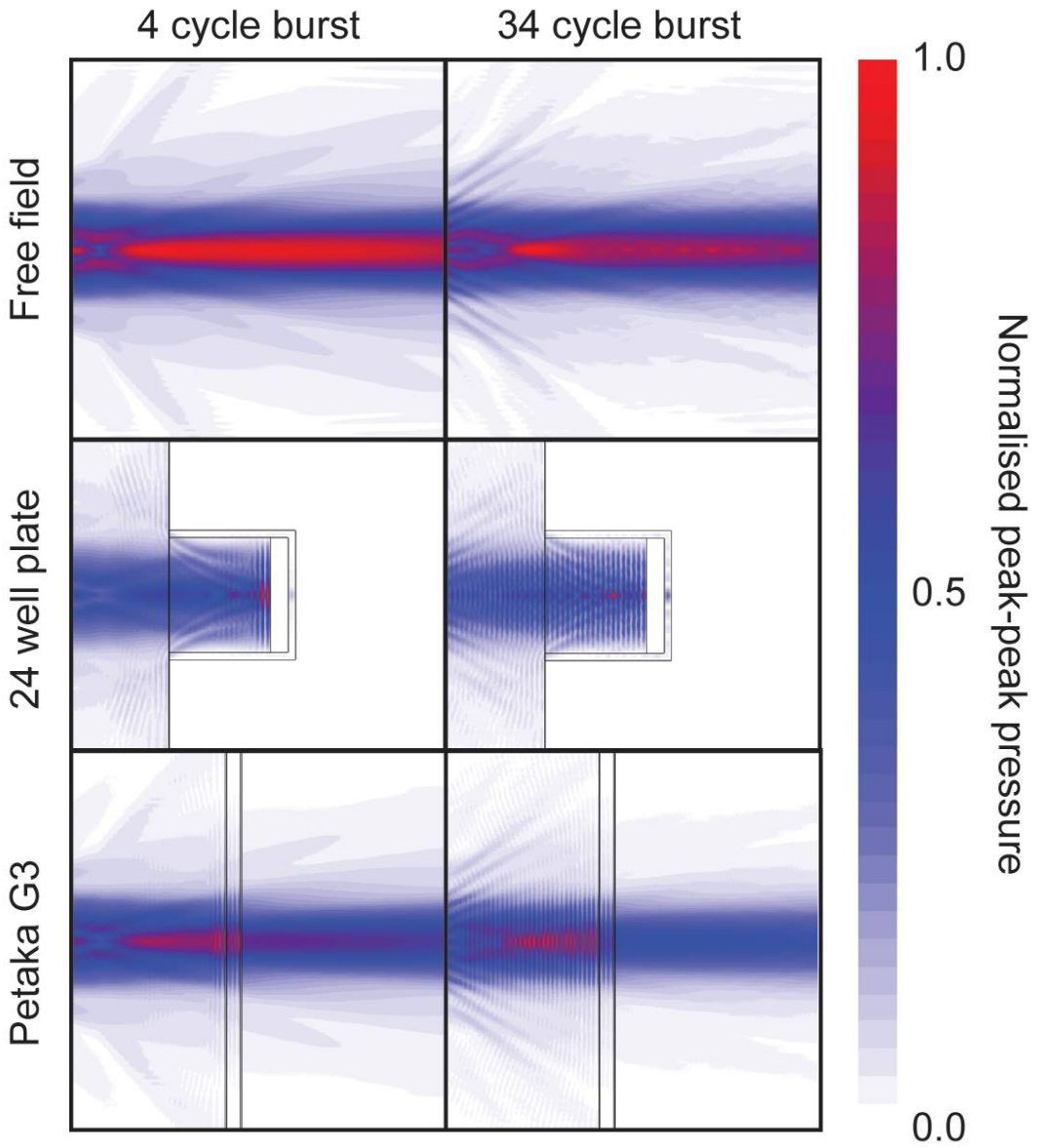

Figure 4.10: Simulation of the ultrasound field generated by the devices. The top fields are the pressure mappings for the transducers in free field conditions. The middle ones are for device A, and the bottom two are for device B.

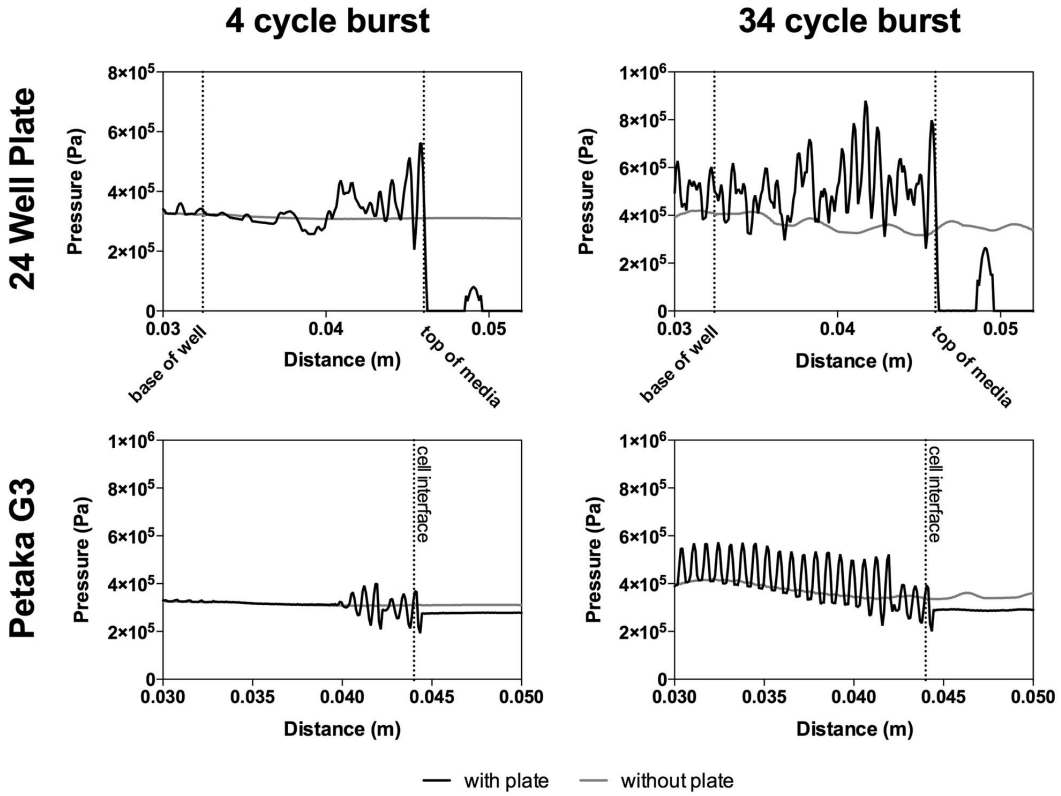

Figure 4.11: Simulated axial pressure values as a function of distance for both devices, the gray line indicates the free field values, the dark line indicates pressures with cell culuture chambers inserted. The vertical dotted lines indicate boundaries. In all cases an increase in pressure was seen when adding the cell culture chambers.

In the 24 well plate, the cells will primarily be floating within the entire cell chamber, hence the sound field inside the entire cell ought to be considered. The 4-cycle burst shows an increase in pressure at the cell culture medium/air-interface, almost 1.5 times higher than that of the free-field analogue. In the 34-cycle burst the pressure was significantly higher, more than doubled at certain locations.

The PetakaG3^{TM} is made primarily for adhered cells, which are attached to the clear plastic walls of the chamber, hence the most important location to evaluate the sound field for these devices is in the immediate proximity of the wall. At a 4-cycle burst, the pressure at this location increased slightly (12%) from that of the free field, and would propagate as the free-field scan, with a slightly reduced

pressure amplitude. With a 34-cycle burst, the change in pressure was less (10%), a very promising result, when compared to the 24-well simulations.

These results indicate an important discrepancy between the free field calibrations typically performed by manufacturers of cell culture-specific ultrasound equipment. Namely, that the acoustic interactions with the devices might cause more than double expected pressures, predicted by the free field calibrations. Nevertheless, these qualitative results need to be confirmed by measurements.

4.9 Future work

A problem discovered with the devices when they were driven for long times on high duty cycles, the TLTs would overheat, and cause a 100% electrical reflection. This could be avoided by submerging the bottom of the plate into a ice bath. However, a more robust solution with larger ferrite cores, or including an active cooling fan, would conserve the portability of the devices, and should be considered when constructing new ones.

The simulations of the acoustic behavior inside the cell culture devices, especially the 24-well plate, showed a significant deviation in the pressure exerted. Verification of the *in situ* simulations by measurements are therefore paramount to perform properly designed sonoporation experiments.

Chapter 5

Conclusion

A procedure to design, construct and characterise multi-element biological ultrasound treatment chambers has been presented. It was shown that following the procedure described to construct the ultrasound transducers it was possible to achieve very similar acoustic pressure outputs from all transducers. Backing materials were characterised in order to create transducers as narrowband as possible, whilst still being electrically insulated, allowing them to be submerged in water. Furthermore, high acoustic impedance backing materials were characterised, allowing creation of future devices with a broader bandwidth and shorter pulse lenghts.

Electrical impedance matching substatinally improved the acoustic performance of all devices, tripling the acoustic pressure output. Simulations showed that the addition of a cell culture chamber significantly affected the pressure profile. Hence, great care needs to be taken, when stating pressure values *in situ*.

The electrical impedance results successfully predicted the output behavior of the transducer. When translating these devices into real world usage, thermal degradation in the TLTs was observed. Hence, further work needs to be done, to improve the stability and performance of these devices.

List of Figures

List of Tables

References

[1] B. W. Stewart and C. P. Wild, "World Cancer Report 2014," Tech. Rep., 2014.

[2] M.-H. Chang, "Hepatitis B Vaccination and Hepatocellular Carcinoma Rates in Boys and Girls," *JAMA*, vol. 284, no. 23, p. 3040, Dec. 2000.

[3] P. Goymer, "Gardasil the perfect guard?" *Nature Reviews Cancer*, vol. 5, no. 11, pp. 840–840, Nov. 2005.

[4] L. L. Villa, R. L. R. Costa, C. A. Petta, R. P. Andrade, K. A. Ault, A. R. Giuliano, C. M. Wheeler, L. A. Koutsky, C. Malm, M. Lehtinen, F. E. Skjeldestad, S.-E. Olsson, M. Steinwall, D. R. Brown, R. J. Kurman, B. M. Ronnett, M. H. Stoler, A. Ferenczy, D. M. Harper, G. M. Tamms, J. Yu, L. Lupinacci, R. Railkar, F. J. Taddeo, K. U. Jansen, M. T. Esser, H. L. Sings, A. J. Saah, and E. Barr, "Prophylactic quadrivalent human papillomavirus (types 6, 11, 16, and 18) L1 virus-like particle vaccine in young women: a randomised double-blind placebo-controlled multicentre phase II efficacy trial." *The Lancet. Oncology*, vol. 6, no. 5, pp. 271–8, May 2005.

[5] D. Lyden, D. R. Welch, and B. Psaila, *Cancer Metastasis: Biologic Basis and Therapeutics, Volume 0.* Cambridge University Press, 2011.

[6] P. C. Gø tzsche and K. J. Jø rgensen, "Screening for breast cancer with mammography." *The Cochrane database of systematic reviews*, vol. 6, p. CD001877, Jan. 2013.

[7] J. P. Kösters and P. C. Gø tzsche, "Regular self-examination or clinical examination for early detection of breast cancer." *The Cochrane database of systematic reviews*, no. 2, p. CD003373, Jan. 2003.

[8] D. L. Nelson and M. M. Cox, "Lehninger Principles of Biochemistry 5th ed." pp. 1–1294, 2008.

[9] *NIH Curriculum Supplement Series.* The Institutes, 2007.

[10] G. M. Cooper, *Elements of Human Cancer.* Jones & Bartlett Learning, 1992.

[11] D. Marmé and N. Fusenig, *Tumor Angiogenesis: Basic Mechanisms and Cancer Therapy.* Springer Science & Business Media, 2007.

[12] "Cancer in Norway 2012," Cancer Registry of Norway, Oslo, Tech. Rep., 2012.

[13] A. E. Chang, P. A. Ganz, D. F. Hayes, T. Kinsella, H. I. Pass, J. H. Schiller, R. M. Stone, and V. Strecher, *Oncology: An Evidence-Based Approach.* Springer Science & Business Media, 2007.

[14] P. Price, K. Sikora, and T. Illidge, *Treatment of Cancer Fifth Edition.* CRC Press, 2008.

[15] R. T. Skeel and S. N. Khleif, *Handbook of Cancer Chemotherapy.* Lippincott Williams & Wilkins, 2011.

[16] B. Allen, L. Marcu, and E. Bezak, *Biomedical Physics in Radiotherapy for Cancer.* Csiro Publishing, 2012.

[17] M. Sheaff and S. Baithun, "Pathological effects of ionizing radiation," *Current Diagnostic Pathology*, vol. 4, no. 2, pp. 106–115, Jun. 1997.

[18] E. Fokas, G. Kraft, H. An, and R. Engenhart-Cabillic, "Ion beam radiobiology and cancer: time to update ourselves." *Biochimica et biophysica acta*, vol. 1796, no. 2, pp. 216–29, Dec. 2009.

[19] F. Pediconi, A. Napoli, L. Di Mare, F. Vasselli, and C. Catalano, "MRgFUS: from diagnosis to therapy." *European journal of radiology*, vol. 81 Suppl 1, pp. S118–20, Oct. 2012.

[20] C. Hill, J. Bamber, and G. ter Haar, *Physical Principles of Medical Ultrasonics*. John Wiley & Sons, 2005.

[21] Y. Keisari, *Tumor Ablation: Effects on Systemic and Local Anti-Tumor Immunity and on Other Tumor-Microenvironment Interactions*. Springer Science & Business Media, 2012.

[22] N. S. Barakat, "Magnetically modulated nanosystems: a unique drug-delivery platform." *Nanomedicine (London, England)*, vol. 4, no. 7, pp. 799–812, Oct. 2009.

[23] A. Jordan, R. Scholz, and P. Wust, "Magnetic fluid hyperthermia (MFH): Cancer treatment with AC magnetic field induced excitation of biocompatible superparamagnetic nanoparticles," *Journal of Magnetism and ...*, vol. 201, no. 1-3, pp. 413–419, Jul. 1999.

[24] M. Johannsen, U. Gneveckow, L. Eckelt, A. Feussner, N. Waldöfner, R. Scholz, S. Deger, P. Wust, S. A. Loening, and A. Jordan, "Clinical hyperthermia of prostate cancer using magnetic nanoparticles: presentation of a new interstitial technique." *International journal of hyperthermia : the official journal of European Society for Hyperthermic Oncology, North American Hyperthermia Group*, vol. 21, no. 7, pp. 637–47, Nov. 2005.

[25] A. Delalande, S. Kotopoulis, M. Postema, P. Midoux, and C. Pichon, "Sonoporation: mechanistic insights and ongoing challenges for gene transfer." *Gene*, vol. 525, no. 2, pp. 191–9, Aug. 2013.

[26] P. Marmottant and S. Hilgenfeldt, "Controlled vesicle deformation and lysis by single oscillating bubbles," vol. 423, no. 6936, pp. 153–156, May 2003.

[27] A. Jordan, R. Scholz, K. Maier-Hauff, M. Johannsen, P. Wust, J. Nadobny, H. Schirra, H. Schmidt, S. Deger, S. Loening, W. Lanksch, and R. Felix, "Presentation of a new magnetic field therapy system for the treatment

of human solid tumors with magnetic fluid hyperthermia," *Journal of Magnetism and Magnetic Materials*, vol. 225, no. 1-2, pp. 118–126, Jan. 2001.

[28] M. Postema, *Fundamentals of Medical Ultrasonics*. CRC Press, 2011.

[29] I. Lentacker, I. De Cock, R. Deckers, S. C. De Smedt, and C. T. W. Moonen, "Understanding ultrasound induced sonoporation: definitions and underlying mechanisms." *Advanced drug delivery reviews*, vol. 72, pp. 49–64, Jun. 2014.

[30] S. Kotopoulis, G. Dimcevski, O. H. Gilja, D. Hoem, and M. Postema, "Treatment of human pancreatic cancer using combined ultrasound, microbubbles, and gemcitabine: a clinical case study." *Medical physics*, vol. 40, no. 7, p. 072902, Jul. 2013.

[31] J. A. Kopechek, H. Kim, D. D. McPherson, and C. K. Holland, "Calibration of the 1-MHz Sonitron ultrasound system." *Ultrasound in medicine & biology*, vol. 36, no. 10, pp. 1762–6, Oct. 2010.

[32] N. Nomikou, Y. S. Li, and A. P. McHale, "Ultrasound-enhanced drug dispersion through solid tumours and its possible role in aiding ultrasound-targeted cancer chemotherapy," *Cancer Letters*, vol. 288, no. 1, pp. 94–98, 2010.

[33] K. Hensel, M. P. Mienkina, and G. Schmitz, "Analysis of ultrasound fields in cell culture wells for in vitro ultrasound therapy experiments." *Ultrasound in medicine & biology*, vol. 37, no. 12, pp. 2105–15, Dec. 2011.

[34] T. Yddal, S. Cochran, O. H. Gilja, M. Postema, and S. Kotopoulis, "Open-source, high-throughput ultrasound treatment chamber." *Biomedizinische Technik. Biomedical engineering*, vol. 60, no. 1, pp. 77–87, Feb. 2015.

[35] L. E. Kinsler, A. R. Frey, A. B. Coppens, and J. V. Sanders, "Fundamentals of Acoustics, 4th Edition," *Fundamentals of Acoustics*, 1999.

[36] R. C. D. o. R. S. Preston and A. P. Laboratory), *Output Measurements for Medical Ultrasound*, 1991.

[37] A. A. Vives, *Piezoelectric Transducers and Applications.* Springer Science & Business Media, 2008.

[38] F. A. Duck, A. Baker, and H. Starritt, *Ultrasound in Medicine.* CRC Press, 1998.

[39] J. T. Bushberg and J. M. Boone, *The Essential Physics of Medical Imaging.* Lippincott Williams & Wilkins, 2011.

[40] V. Gibbs, D. Cole, and A. Sassano, *Ultrasound Physics and Technology: How, Why and When.* Elsevier Health Sciences, 2009.

[41] R. Goldberg, M. Jurgens, D. Mills, C. Henriquez, D. Vaughan, and S. Smith, "Modeling of piezoelectric multilayer ceramics using finite element analysis," *IEEE Transactions on Ultrasonics, Ferroelectrics and Frequency Control*, vol. 44, no. 6, pp. 1204–1214, Nov. 1997.

[42] K. Uchino, *Piezoelectric Actuators and Ultrasonic Motors.* Springer Science & Business Media, 1997.

[43] L. Callegaro, *Electrical Impedance: Principles, Measurement, and Applications.* CRC Press, 2012, vol. 6.

[44] J. Huang, *AC/DC Power System Small-signal Impedance Measurement for Stability Analysis.* ProQuest, 2009.

[45] T. A. Milligan, *Modern Antenna Design.* John Wiley & Sons, 2005.

[46] D. J. Griffiths, *Introduction to Electrodynamics.* Prentice Hall, 1999.

[47] "Ultrasonics - Hydrophones - Part 1: Measurement and characterization of medical ultrasonic fields up to 40 MHz," *IEC 62127-1ed1.1 Consol. with am1*, p. 178, 2013.

[48] R. Lerch, "Ultrasound fields in attenuating media," *The Journal of the Acoustical Society of America*, vol. 80, no. 4, p. 1140, Oct. 1986.

[49] S. Rajagopal, N. Sadhoo, and B. Zeqiri, "Reference Characterisation of Sound Speed and Attenuation of the IEC Agar-Based Tissue-Mimicking Material Up to a Frequency of 60 MHz." *Ultrasound in medicine & biology*, pp. 1–17, Sep. 2014.

[50] C. Sun, S. D. Pye, J. E. Browne, A. Janeczko, B. Ellis, M. B. Butler, V. Sboros, A. J. W. Thomson, M. P. Brewin, C. H. Earnshaw, and C. M. Moran, "The speed of sound and attenuation of an IEC agar-based tissue-mimicking material for high frequency ultrasound applications." *Ultrasound in medicine & biology*, vol. 38, no. 7, pp. 1262–70, Jul. 2012.

[51] S. Kotopoulis, H. Wang, S. Cochran, and M. Postema, "Lithium niobate transducers for MRI-guided ultrasonic microsurgery," *IEEE Transactions on Ultrasonics, Ferroelectrics, and Frequency Control*, vol. 58, no. 8, pp. 1570–1576, 2011.

[52] D. A. Hall and P. J. Stevenson, "High field dielectric behaviour of ferroelectric ceramics," *Ferroelectrics*, vol. 228, no. 1, pp. 139–158, May 1999.

[53] Q. M. Zhang and J. Zhao, "Electromechanical properties of lead zirconate titanate piezoceramics under the influence of mechanical stresses." *IEEE transactions on ultrasonics, ferroelectrics, and frequency control*, vol. 46, no. 6, pp. 1518–1526, 1999.

[54] T. Bove, D. Damjanovic, K. Liang, and W. Wolny, "Piezoceramic materials for high-temperature & high-pressure applications in oilfield exploration & production," in *2013 Joint IEEE International Symposium on Applications of Ferroelectric and Workshop on Piezoresponse Force Microscopy (ISAF/PFM)*. IEEE, Jul. 2013, pp. 62–65.

[55] "Agar Scientific Silver Epoxy data sheet."

[56] J. Sewick, *Transmission Line Transformers*, 4th ed. Atlanta, GA: Noble Publishing Corporation, 2001.

[57] ——, *Transmission Line Transformers Handbook*, Amidon, Ed., 1997.

[58] "3M Glass Bubbles K Series, S Series and iM Series."

[59] R. Weast, M. Astle, and W. Beyer, *CRC handbook of chemistry and physics*, 1988.

[60] J. B. Fowlkes, "Systems for degassing water used in ultrasonic measurements," *The Journal of the Acoustical Society of America*, vol. 90, no. 2, p. 1197, Aug. 1991.

[61] J. W. Hunt, M. Arditi, and F. S. Foster, "Ultrasound transducers for pulse-echo medical imaging." *IEEE transactions on bio-medical engineering*, vol. 30, no. 8, pp. 453–481, 1983.

[62] K. Raum and W. D. O'Brien Jr., "Pulse-echo field distribution measurement technique for high-frequency ultrasound sources," *IEEE Transactions on Ultrasonics, Ferroelectrics and Frequency Control*, vol. 44, no. 4, pp. 810–815, 1997.

[63] M. X. Tang and R. J. Eckersley, "Frequency and pressure dependent attenuation and scattering by microbubbles," *Ultrasound in Medicine and Biology*, vol. 33, no. 1, pp. 164–168, 2007.

[64] A. Bernassau, D. Hutson, C. Demore, and S. Cochran, "Characterisation of an epoxy filler for piezocomposite material compatible with microfabrication processes," in *2008 IEEE Ultrasonics Symposium*. IEEE, Nov. 2008, pp. 62–65.